

Superacid *In Situ* Protected Synthesis of Covalent Organic Frameworks

Xingyao Ye,[‡] Ruoyang Liu,[‡] Xinyu Mu, Shanshan Tao, Hao Yang, Xuejiao J. Gao, Shuo-Wang Yang, and Donglin Jiang^{*}



Cite This: *J. Am. Chem. Soc.* 2025, 147, 6942–6957



Read Online

ACCESS |

Metrics & More

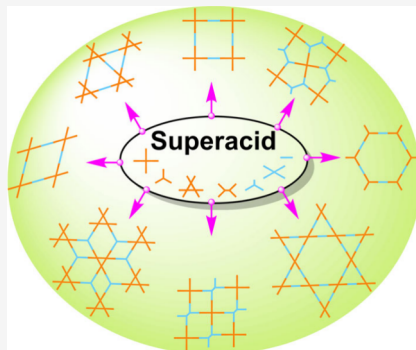


Article Recommendations



Supporting Information

ABSTRACT: Covalent organic frameworks, as a class of fascinating crystalline porous materials, are attracting increasing attention in various fields. Synthesizing these materials to attain crystallinity and porosity is essential; however, it is time-consuming, not cost-effective, and energy-demanding as it involves extensive screenings of reaction conditions and employs undesired aromatic solvents. Despite recent progress in the synthesis, finding an efficient, convenient, low-toxicity, and widely applicable method remains a challenging goal. Here, we report an *in situ*-protected strategy for synthesizing imine-linked frameworks by exploring triflic acid as the catalyst to replace traditional acetic acid and deploying alcohols as a single-component reaction medium instead of aromatic solvents. We found that the function of triflic acid is threefold: it rapidly protonates amino groups of amine monomers into ammonium cations, protects formyl units of aldehyde monomers by converting them into acetals, and improves the solubilities of both monomers. The *in situ*-protection scheme greatly changes their concentrations and reactivities, making reactions highly controllable and reversible. This strategy is general for various monomer combinations to develop imine-linked frameworks with different topologies, including tetragonal, rhombic, pentagonal, hexagonal, kagome, dual trigonal, dual rhombic, and dual hexagonal shapes, and various pore sizes from micropores to mesopores, presenting a facile and simple way to synthesize 28 different yet high-quality frameworks in *n*-butanol/water. Remarkably, nine new imine-linked frameworks are synthesized for the first time, which cannot be prepared by traditional systems. The porphyrin frameworks exhibited exceptional photocatalytic activities in the activation of molecular oxygen to produce highly reactive oxygen species of singlet oxygen.



1. INTRODUCTION

Covalent organic frameworks (COFs) are a class of crystalline and porous polymers that enable predesigned integration of organic building units into well-defined polygonal skeletons and aligned discrete pores.^{1–10} Most strikingly, both skeleton and pore can be molecularly predesigned and synthetically controlled; the skeleton is predetermined by topology diagram, while the pore, i.e., its pore size, shape, and environment, can be controlled by monomer structures. This distinct feature presents fundamental differences with other inorganic- or metal-based frameworks and amorphous organic materials. The unique presence of COFs directs a strong driving force worldwide from different fields into the exploration of their structures, properties, and applications. COFs merge stability with π -electronic diversity and rich porosity, setting an irreplaceable platform for establishing structure–property correlations and discovering structure-originated properties and functions.^{1–10}

COFs are synthesized through concurrent polycondensation of monomers into polygonal backbones and supramolecular polymerization of these backbones into extended yet ordered structures along the *x*, *y*, and *z* directions. Among various polycondensation reactions, imine polycondensation using

aldehyde and amine as reactive groups is the most widely explored owing to the structural diversity of both aldehyde and amine monomers.^{1–3} Preparation of COFs with crystallinity and porosity is not a simple task; this has been proved true by many experiments, as a slight variation of knot, linker, and/or even a substituent on building blocks would greatly change the reactions, most probably resulting in the formation of amorphous cross-linked polymers ending with unclear structures.

A general yet established measure is to screen the reaction conditions extensively, as we termed six tables in our laboratory, including mixed solvents and their ratios (two tables), catalysts and their concentrations (two tables), reaction temperature (one table), and reaction time (one table). The combination of these conditions would be as many as possible to identify the proper zone that enables the one-pot

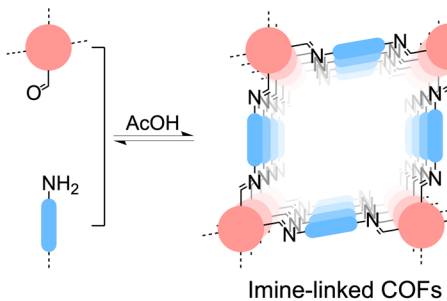
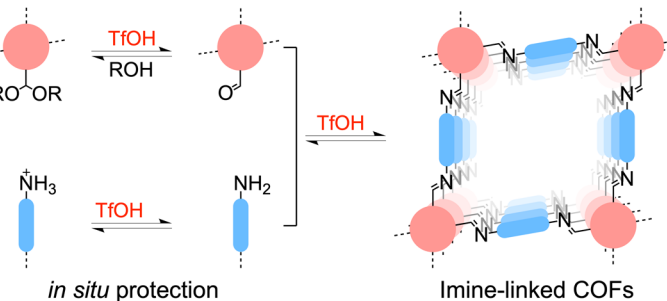
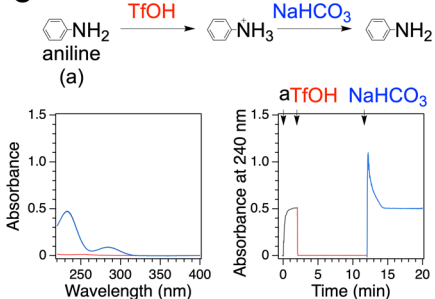
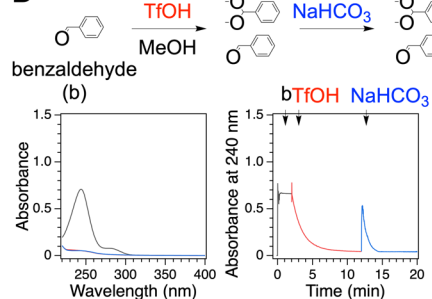
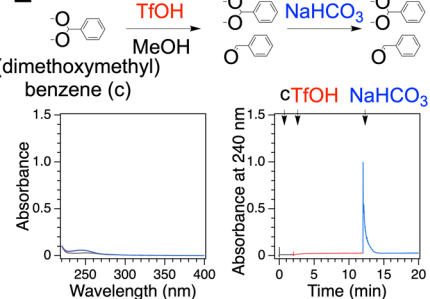
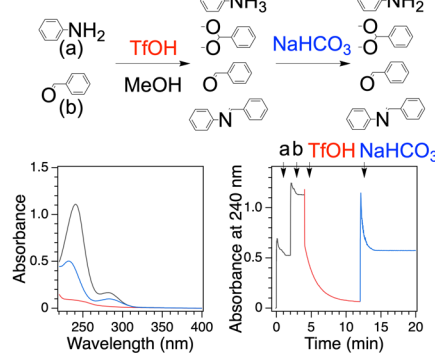
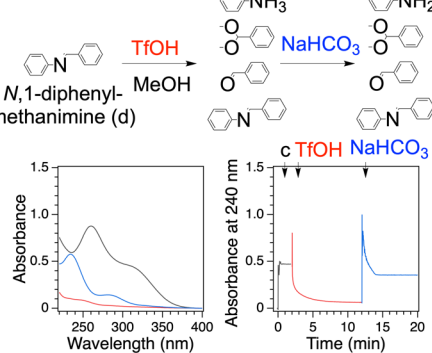
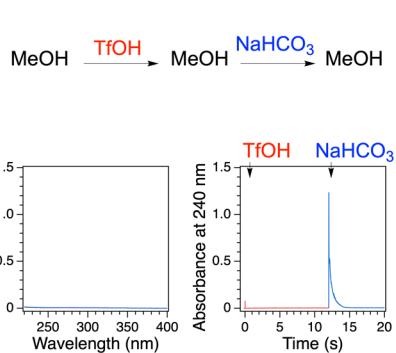
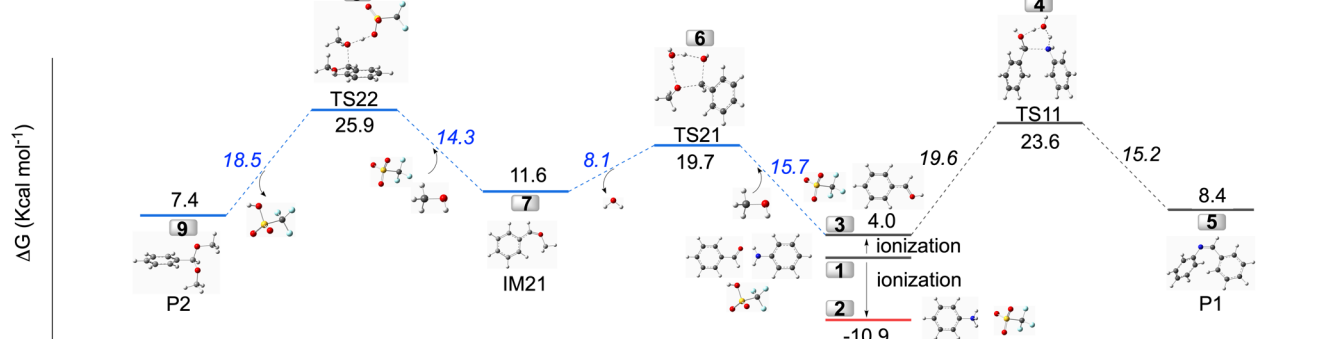
Received: December 9, 2024

Revised: February 1, 2025

Accepted: February 3, 2025

Published: February 12, 2025



A Conventional Method**B This Strategy****C****D****E****F****G****H****I**

- 1 aniline + benzaldehyde + TfOH + 2 MeOH + H₂O
 ■ 2 benzenaminium + benzaldehyde + TfO⁻ + 2 MeOH + H₂O
 ■ 3 aniline + benzylideneoxonium + TfO⁻ + 2 MeOH + H₂O
 ■ 4 TS11 + TfO⁻ + 2 MeOH
 ■ 5 P1 + TfOH + 2 MeOH + 2 H₂O
 ■ 6 aniline + TS21 + TfO⁻ + MeOH
 ■ 7 aniline + IM21 + TfO⁻ + MeOH + 2 H₂O
 ■ 8 aniline + TS22 + 2 H₂O
 ■ 9 aniline + P2 + TfOH + 2 H₂O

Figure 1. Concept and model reactions. (A) Conventional strategy for imine-linked COFs via AcOH catalysis. (B) New strategy for imine-linked COFs via superacid TfOH catalysis. (C–H) Model reactions with (C) aniline, (D) benzaldehyde, (E) (dimethoxymethyl)benzene, (F) aniline and benzaldehyde, (G) N,1-diphenylmethanimine, and (H) blank control (Top panel for scheme upon addition of TfOH and NaHCO₃; bottom panel left plot: Electronic absorption spectral change from the original (black) to the ones upon addition of TfOH (red) and NaHCO₃ (blue); bottom panel right plot: time-dependent absorbance change from the original (black) to ones upon addition of TfOH (red) and NaHCO₃ (blue)). (I) Theoretical reaction pathway of the model reaction.

complex reaction to grow well-defined crystalline porous frameworks with the highest structural integrity. In many cases, searching for the optimal conditions for a specific COF is

tedious, time-consuming, energy-demanding, and not cost-effective laboratory work. An exception is the iconic COFs, i.e., the imine-linked TPB-DMTP-COF,¹¹ which features high

stability, crystallinity, and porosity that can be attained over a wide range of reaction conditions. A narrow reaction condition results in an unbalance in the quality control of COFs between groups even synthesized under identical conditions.

In this study, we report a new strategy based on an *in situ*-protected scheme for the synthesis of imine-linked COFs. By exploring a superacid, i.e., triflic acid (TfOH), as the catalyst, we found that TfOH behaves completely differently from conventional catalysts, including acetic acid (AcOH), trifluoroacetic acid, *para*-toluenesulfonic acid (PTSA), or Lewis acid. We observed that TfOH functions in three ways: (1) It swiftly protonates the amino group of amine monomers into ammonium cations. (2) It protects the formyl sites of aldehyde monomers by converting them into acetals. (3) Owing to these two *in situ* reactions, it improves the solubilities of both protected amine and aldehyde monomers, which become highly soluble in alcohols and even water. This allows us to develop single-component alcohol as the solvent, enabling us to exclude the use of high-boiling-point yet toxic aromatic reagents as solvents. Through detailed studies on the systems by fixing the primary reaction conditions at the TfOH–alcohol combination, we found the following seven key aspects.

(1) TfOH is essential for polymerization: TfOH enables *in situ* protection of both monomers and enhances their solubilities, which greatly improves the reaction reversibility and decreases the reaction kinetics, yielding high-quality COFs.

(2) The concentration of TfOH is key: An optimal concentration exists between 0.006 and 0.016 M in the reaction mixture which operates well for all syntheses, while lower concentrations result in insufficient protection, and higher concentrations cause a drastic drop in reaction rate and yield.

(3) Alcohol as the sole solvent: This is a marvelous advance by using alcohols as the solvent; MeOH, EtOH, *n*-propanol, *n*-BuOH, *tert*-BuOH, *n*-pentanol, *n*-hexanol, *n*-octanol, and *n*-decanol work well, excluding the necessity of aromatic solvents.

(4) High temperature improves crystallinity: High temperatures promote polycondensation and improve crystallinity.

(5) Wide applicability: This strategy is general for the synthesis of imine-linked COFs with different topologies and pore sizes. We demonstrate the applicability with 28 COF examples.

(6) Breaking through the limit of the traditional method: This strategy enables the synthesis of nine new COFs, which are unprecedented and/or cannot be synthesized by conventional methods.

(7) Exceptional photocatalysis: Two porphyrin COFs with *mcm* and *cpq* topologies achieve exceptional activities in the photocatalytic activation of molecular oxygen to produce singlet oxygen.

These new findings and insights not only reveal a new scheme for COF synthesis but also offer a general yet transformative way to explore unprecedented COFs for structural and functional discovery.

2. RESULTS AND DISCUSSION

2.1. Basic Concept. The synthesis of COFs usually employs monomers with rigid π backbones, which assume a topology-directed connection of building units when they form covalent bonds. These π monomers are poorly soluble in common organic solvents and water, leading to the necessity of using high-boiling-point aromatic solvents for reactions. A

slight structural change in the π scaffold or even a minor alteration in the side substituent would greatly change solubilities as well as reactivities, adding further difficulties to the originally complex reaction system consisting of both polycondensation and supramolecular polymerization. This endows the synthesis of COFs with a general feature that a systematic screening of reaction conditions, including solvent, catalyst, reaction temperature, and reaction time, is necessary for each combination of knot and linker units. Notably, even upon extensive condition screenings, many combinations of monomers cannot yield crystalline porous frameworks, although they are topologically allowed, highlighting another distinct feature of the synthetic challenge.

To address these general issues, our basic idea is twofold: (1) The first one is to improve the solubilities of both monomers. This concept comes from the traditional systems where monomers are not well-dissolved; we assume a soluble system would exclude the possibility of crystallization of oligomers on undissolved solid surfaces. (2) The second method is to reduce the reaction rate to enable timely and sufficient structural self-healing during the reaction. However, these two effects are contradictory to merge into one system, which was unprecedented in COF synthesis. In this study, we found that a superacid, i.e., TfOH, meets these two aspects simultaneously and unexpectedly enables us to develop a new synthetic strategy.

For the imine-linked COFs, AcOH is the most widely used (Figure 1A); meanwhile, aromatic solvents such as mesitylene, *o*-dichlorobenzene (*o*-DCB), and xylene are commonly used as an essential component for the mixed solvent.^{6,9,11} In sharp contrast, in the case of superacid TfOH, both monomers become soluble upon *in situ*-protection reactions, keeping both monomers in their protected forms, reducing the reaction rate, and eliminating the use of aromatic solvents (Figure 1B). On the other hand, the superacid presents strong acidic conditions, which facilitate backward reactions to enable timely yet sufficient self-healing of structural defects. This distinct form of the preprotection method,^{12–15} which can change the solubility of monomers before the reaction starts, but with the progress of the polymerization catalyzed by AcOH, eventually behaves the same as the conventional AcOH-catalyzed nonprotected systems. In contrast, our *in situ* one-pot protection strategy triggers profound effects on the existence of monomer forms (see below), reduces forward polymerization, and facilitates self-healing reactions.

2.2. Model Reactions. To disclose why TfOH works differently from AcOH and elucidate the mechanism of TfOH-catalyzed reaction, we conducted five model reactions, including (1) protonation of aniline in the presence of TfOH; (2) protection of benzaldehyde by TfOH in the presence of alcohol; (3) reaction of (dimethoxymethyl)-benzene with TfOH, which is the reverse reaction of 2; (4) condensation between aniline and benzaldehyde by TfOH; and (5) the reaction of *N*,*1*-diphenylmethanimine with TfOH, which is the reverse reaction of 4. We conducted electronic absorption spectroscopy, as it is very sensitive for monitoring the changes of chemical species. We monitored the absorption band at 240 nm of the mixture of aniline and benzaldehyde to reveal the time-dependent change in chemical species. Meanwhile, we calculated the composition ratio from the absorbance difference in the presence and absence of TfOH. We added saturated NaHCO₃ aqueous solution when these reaction groups reached the balance after the addition of

TfOH. The neutralization only influenced the protonation of aniline and helped to calculate the protonation yield.

(1) TfOH protonates aniline quantitatively (**Figure 1C**): Adding TfOH (0.2 M) to aniline triggers an abrupt drop of absorbance at 233 nm within 3 s (**Figure 1C**, bottom panel figures, red curve). ¹H NMR spectroscopy confirmed the formation of benzenaminium (**Figure S1A,B**), with disappeared peak from $-\text{NH}_2$ (4.64 ppm), appeared peak of $-\text{NH}_3^+$ (7.36–7.40 ppm), and shifted peak from phenyl ring (from 6.69–6.76 to 7.30–7.32 ppm, and from 7.09–7.13 to 7.47–7.51 ppm). Notably, benzenaminium was reversed to aniline upon neutralization with NaHCO₃, recovering both the original spectrum and absorbance (**Figure 1C**, bottom panel figures, blue curve). Notably, the protonation proceeds well in solvents such as *n*-BuOH, dioxane, and acetonitrile (MeCN) to achieve quantitative yields (**Figure S2A,F,K**). In contrast, acetic acid (6 M) allows aniline protonation to reach only a 26% yield (**Figure S3A**).

(2) TfOH protects benzaldehydes with acetals (**Figure 1D**): In the presence of TfOH (0.2 M) and MeOH, benzaldehyde forms acetal, i.e., (dimethoxymethyl)benzene in 81% yield, as revealed by the absorption spectral change (**Figure 1D**, bottom panel figures, red curve) and 73% yield as shown in ¹H NMR spectroscopy (**Figure S1C,D**). The acetal formation proceeds only in the presence of alcohols and TfOH; this reaction cannot be reversed by adding NaHCO₃ (**Figure 1D**, bottom panel figures, blue curve; **Figure S2B,G,L**; **Figure S3B**).

(3) TfOH reverses (dimethoxymethyl)benzene to benzaldehyde (**Figure 1E**): (Dimethoxymethyl)benzene upon the addition of TfOH generates benzaldehyde in 19% yield (**Figure 1E**, bottom panel figures, red curve), while the further addition of NaHCO₃ did not change the system (**Figure 1E**, bottom panel figures, blue curve). Therefore, an equilibrium between (dimethoxymethyl)benzene and benzaldehyde is established by TfOH in a ratio of 81:19 at room temperature.

(4) TfOH slows the imine formation from aniline and benzaldehyde (**Figure 1F**): Without the addition of acid, the yield of *N*,1-diphenylmethanimine is 49% as revealed by the absorbance difference (**Figure 1F**, bottom panel figures, black curve) and 68% as calculated from ¹H NMR spectroscopy (**Figure S1E**). In the presence of TfOH (0.2 M), the yield of *N*,1-diphenylmethanimine was reduced to 8%, 92% aniline was stored as benzenaminium, 82% benzaldehyde was saved as acetal, while 10% benzaldehyde remained unreacted, as revealed by the spectral change (**Figure 1F**, bottom panel figures, red curve). As shown in ¹H NMR spectroscopy (**Figure S1E,F**), the typical signals of imine linkages at 8.58 ppm and signals of aniline (4.61 ppm for $-\text{NH}_2$ and 6.69–6.75 ppm for C–H of phenyl rings) disappeared after the addition of TfOH, indicating that hydrolysis and protonation happened. Additionally, the molar ratio of benzaldehyde and (dimethoxymethyl)benzene was 1/1.25 in the presence of TfOH (0.2 M, 10 vol %) and benzenaminium. In the case of AcOH catalyst, 72% aniline and benzaldehyde reacted to form *N*,1-diphenylmethanimine, while 12% aniline was stored as benzenaminium, and 16% aniline and 28% benzaldehyde remained unreacted (**Figure S3D**). Therefore, the imine formation reaction is greatly slowed down by TfOH while concurrently retaining monomers in their protected forms of benzenaminium and (dimethoxymethyl)benzene. Neutralization of the system with NaHCO₃ only reversed benzenaminium back to aniline (**Figure 1F**, bottom panel figures, blue curve; **Figure S2C,H,M**; **Figure S3D**).

(5) TfOH promotes the reaction from *N*,1-diphenylmethanimine to benzenaminium, (dimethoxymethyl)benzene, and benzaldehyde (**Figure 1G**): TfOH facilitates the formation of 92% benzenaminium, 82% (dimethoxymethyl)benzene, and 10% benzaldehyde from *N*,1-diphenylmethanimine (**Figure 1G**, bottom panel figures, red curve), which is the reverse reaction of the imine formation reaction. This result indicates that TfOH promotes the reverse reaction, facilitating the self-healing of structural defects during the polymerization. In contrast, AcOH facilitates the formation of 12% benzenaminium, 16% aniline, and 28% benzaldehyde from *N*,1-diphenylmethanimine (**Figure S3E**).

(6) Blank control (**Figure 1H**): The absorbance of MeOH solution upon addition of TfOH followed by addition of NaHCO₃ did not change, eliminating any background in the monitoring (**Figure 1H**, bottom panel figures; **Figure S2E,J,O**). The jump in the absorbance upon the addition of NaHCO₃ originates from the formation of insoluble salts, which eventually precipitate to form a clear solution. As the AcOH system exhibited a weak absorption (0.094 and 0.012, respectively; **Figure S3F**), their absorbances were deducted in the yield calculation and time-dependent spectral change (**Figure S3**).

These detailed model studies revealed that the following three key reactions concurrently occurred in the TfOH system: (1) protonation of aniline, (2) acetal formation, and (3) slowed down imine condensation between aniline and benzaldehyde. Among them, reactions 1 and 2 protect reactive sites and store monomers in their protected forms, which slow down the reaction rate. This enables the release of monomers in a manageable way. Remarkably, reaction 3 is highly reversible as evidenced by a low yield of 8% *N*,1-diphenylmethanimine, enabling timely self-healing of defects during polymerization.

2.3. Reaction Mechanism. We revealed the model reaction mechanism by DFT calculations (**Figure 1I**). (i) Protonation of aniline (**Figure 1I**, 1 → 2) is spontaneous in the presence of TfOH due to its strong acidity and forms benzenaminium triflate, whose energy level is $-10.9 \text{ kcal mol}^{-1}$ lower than that of aniline. (ii) Acetal formation goes through three steps (1 → 3 → 7 → 9) with two transition states (6 and 8), including protonation of benzaldehyde (1 → 3), formation of hemiacetal intermediate (3 → 6 → 7), and formation of the final acetal forms (7 → 8 → 9). The energy level of benzylideneoxonium triflate (3) is only 4 kcal mol^{-1} higher than that of benzaldehyde (1). Benzylideneoxonium triflate overcomes an energy barrier of 15.7 kcal mol^{-1} to form hemiacetal intermediate (7; 11.6 kcal mol^{-1}). The formation of acetal follows (9; 7.4 kcal mol^{-1}). This step climbs a 14.3 kcal mol^{-1} energy barrier. (iii) The formation of *N*,1-diphenylmethanimine requires two steps (1 → 3 → 5) with one transition state (4). The first one is the same protonation of benzaldehyde (1 → 3, 1-diphenylmethanimine requires two steps (1 → 3 → 5) with one transition state (4). The first one is the same protonation of benzaldehyde (1 → 3), while the second one is a nucleophilic attack by aniline (3 → 4). This step conquers an energy barrier of 19.6 kcal mol^{-1} to form *N*,1-diphenylmethanimine (5; 8.4 kcal mol^{-1}).

Based on the above results, we concluded the following distinct points. (i) Protonation, acetal reaction, and imine formation are all fully reversible reactions even at room temperature in the presence of TfOH, as the energy barrier of each step is lower than 20 kcal mol^{-1} . (ii) Acetal formation is

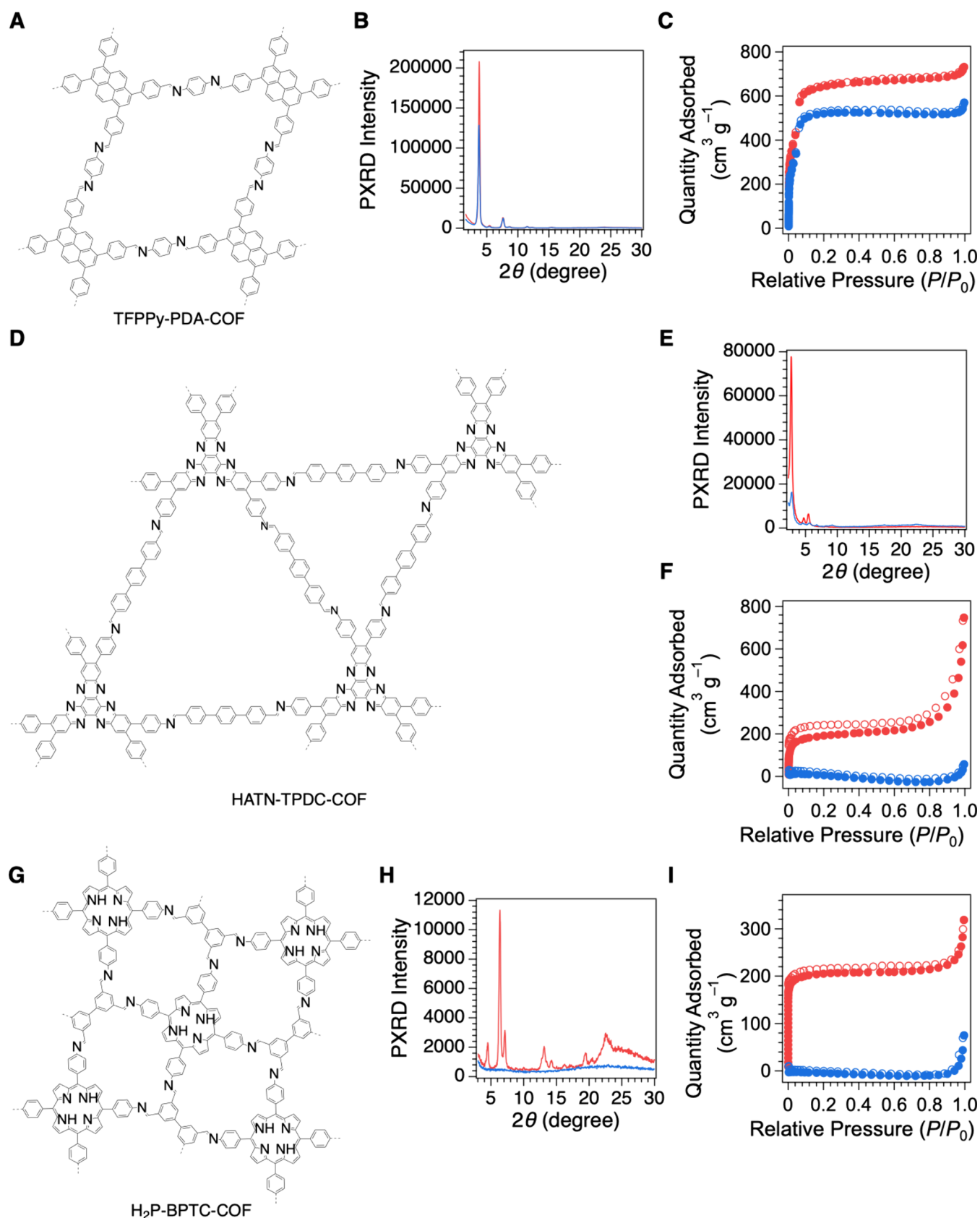


Figure 2. Typical examples of COFs. (A–C) TFPPy-PDA-COF: (A) Scheme, (B) PXRD, and (C) N₂ sorption isotherms. (D–F) HATN-TPDC-COF: (D) Scheme, (E) PXRD, and (F) N₂ sorption isotherms. (G–I) H₂P-BPTC-COF: (G) Scheme, (H) PXRD, and (I) N₂ sorption isotherms. In B, C, E, F, H, and I, red curves are for TfOH, while blue ones are for AcOH.

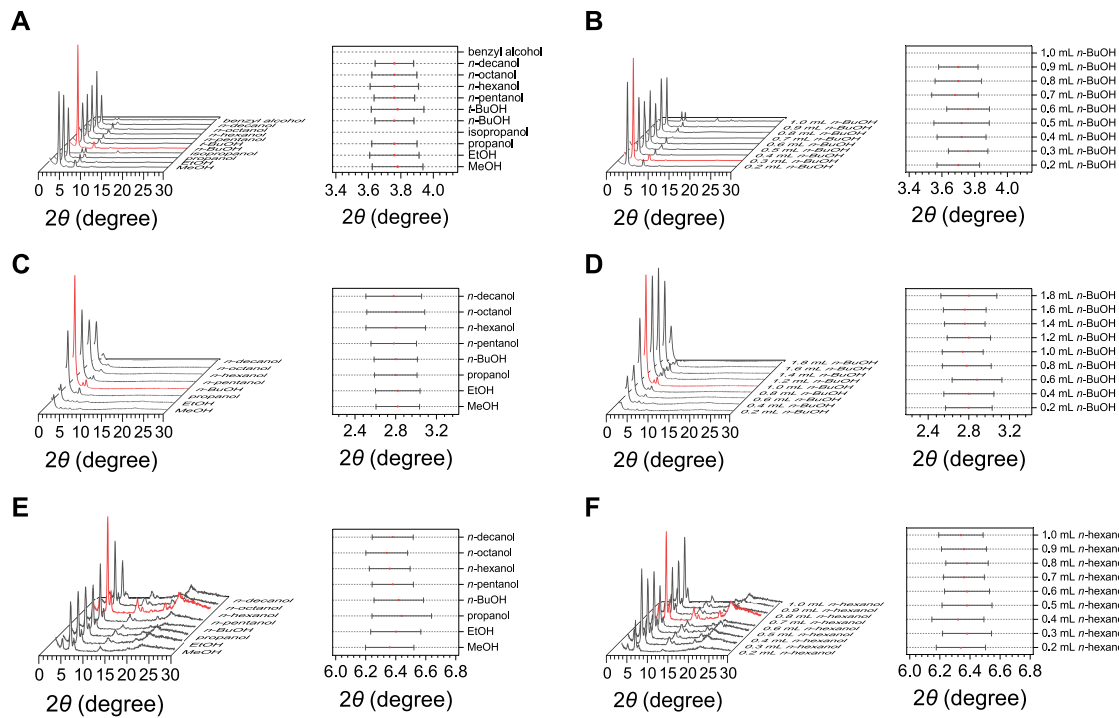


Figure 3. Key polymerization parameters. (A–F) PXRD patterns (left) and fwhm charts (right) of TFPPy-PDA-COF (A, B), HATN-TPDC-COF (C, D), and H₂P-BPTC-COF (E, F). (PXRD patterns: red, the best condition; black, the other conditions; FWHW bar charts: red spots, centered peak position; black line, fwhm.)

competitive with imine formation as the energy barrier of the hemiacetal intermediate is 3.9 kcal mol⁻¹ lower than that of N,1-diphenylmethanimine, though the energy level of the hemiacetal intermediate is slightly higher than that of N,1-diphenylmethanimine. We did not detect the hemiacetal intermediate in the NMR spectra, because the energy barriers between the three acetal steps are both low, while the acetal products are thermodynamically more stable. (iii) The protonated aniline and acetal form of aldehyde are thermodynamically favored states compared to imine model compound, which indicates the strength of protection reaction and matches with the experimentally observed yields. As for the COF synthesis, the imine products precipitate from the solution when they reached high molecular weight, providing an external force forwarding the chemical equilibriums to the imine products.

2.4. Unique Features. Taking three COFs as typical examples (Figure 2; Tables S1–S4), i.e., rhombic TFPPy-PDA-COF (Figure 2A–C; Tables S1 and S2; Figure S6A,D), trigonal HATN-TPDC-COF (Figure 2D–F; Tables S1 and S3; Figure S6B,E), and pentagonal H₂P-BPTC-COF (Figure 2G–H; Tables S1 and S4; Figure S6C,F), we revealed unique features of this new strategy.

(1) Rhombic TFPPy-PDA-COF: The conventional AcOH catalytic systems¹⁶ yielded the COF with good crystallinity by showing a powder X-ray diffraction (PXRD) intensity of 127.1 K (Figure 2B, blue curve; Table S1) with the full width of half-maximum (fwhm) of 0.299°, together with a good porosity (Figure 2C, blue dots; Table S1) with a Brunauer–Emmett–Teller (BET) surface area of 1697 m² g⁻¹ and a pore volume of 0.79 cm³ g⁻¹ (Table S1; Figure S6A, D, blue and gray). Surprisingly, the superacid TfOH system produces TFPPy-PDA-COF with an enhanced PXRD intensity of 208.6 K (Figure 2C, red curve; Tables S1 and S2) with a narrow fwhm

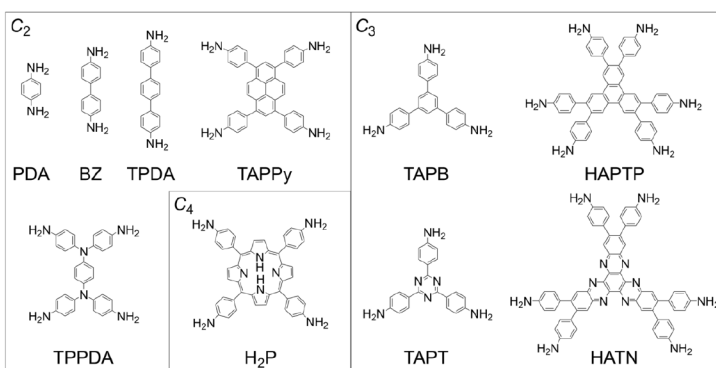
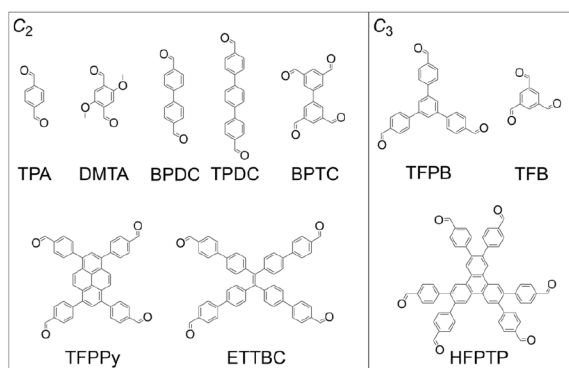
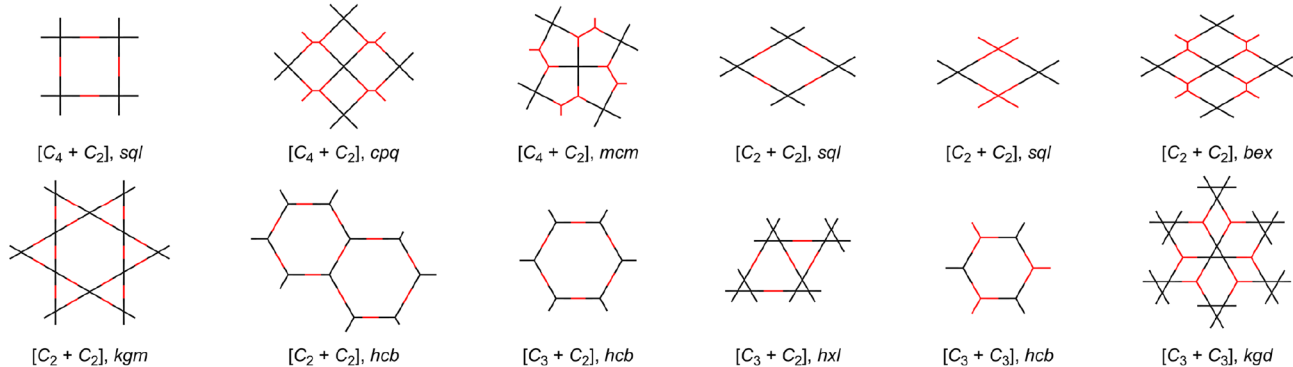
of 0.241°, an increased BET surface area of 2163 m² g⁻¹, and an improved pore volume of 1.02 cm³ g⁻¹ (Figure 2C, red dots; Table S1; Figure S6A, D, red and black). These results unambiguously revealed that TfOH grows TFPPy-PDA-COF with much higher crystallinity and porosity.

(2) Trigonal HATN-TPDC-COF: The AcOH system generates a low PXRD intensity of 16.3 K (Figure 2E, blue curve; Tables S1 and S3) and no porosity (Figure 2F, blue dots; Table S1). In contrast, TfOH greatly improves the PXRD intensity to 77.9 K (Figure 2E, red curve; Tables S1 and S3), the BET surface area to 655 m² g⁻¹, and the pore volume to 0.22 cm³ g⁻¹ (Figure 2F, red dots; Table S1; Figure S6B, E). These results suggest that TfOH facilitates not only skeleton growth but also pore development.

(3) Pentagonal H₂P-BPTC-COF: The AcOH approach results in only amorphous polymers without crystallinity (Figure 2H, blue curve; Tables S1 and S4) and no porosity (Figure 2I, blue dots; Table S1). In sharp contrast, superacid TfOH greatly enhanced the PXRD intensity to 10.6 K (Figure 1H, red curve; Tables S1 and S4), the BET surface area to 638 m² g⁻¹, and the pore volume to 0.29 cm³ g⁻¹ (Figure 2I, red dots; Table S1; Figure S6C, F). These contrasting results reflect that superacid TfOH allows the synthesis of crystalline porous COFs, which cannot be developed through conventional AcOH systems.

With these typical examples in mind, we explored the systems broadly and revealed the key reaction parameters of the superacid system for the facile synthesis of high-quality COFs.

2.5. Key Reaction Parameters. We focused on the above three COFs to screen reaction conditions with an aim to reveal the key reaction parameters in superacid TfOH-catalyzed COF synthesis. We deployed PXRD intensity and fwhm of the highest peak ((110) peak of TFPPy-PDA-COF, (100) peak of

AAmine ($-NH_2$) MonomersAldehyde ($-CHO$) Monomers**B****C**

No.	COF	AcOH ^{ref}	TfOH	Topology	Figure	No.	COF	AcOH ^{ref}	TfOH	Topology	Figure	
[C ₄ + C ₂]												
1	H ₂ P-TPA-COF	✓ ^{17,18}	✓	Tetra	5A, S11		4	H ₂ P-ETTBC-COF	✓ ^{21,22}	✓	D Rhom	5D, S14
2	H ₂ P-DMTA-COF	✓ ¹⁹	✓	Tetra	5B, S12		5	H ₂ P-BPTC-COF	✓	✓	Penta	5E, S15
3	H ₂ P-BPDC-COF	✓ ^{18,20}	✓	Tetra	5C, S13							
[C ₂ + C ₂]												
6	TAPPY-TPA-COF	✓ ^{23,24}	✓	Rhom	6A, S16		13	TAPPY-TFPPy-COF	✓ ²⁹	✓	Rhom	6H, S23
7	TAPPY-DMTA-COF	✓ ^{24,25}	✓	Rhom	6B, S17		14	TAPPY-ETTBC-COF	✓	✓	D Rhom	6I, S24
8	TAPPY-BPDC-COF	✓ ^{24,26}	✓	Rhom	6C, S18		15	TAPPY-BPTC-COF	✓	✓	D Rhom	6J, S25
9	TAPPY-TPDC-COF	✓	✓	Rhom	6D, S19		16	TPPDA-TFPPy-COF	✓ ³⁰	✓	D Rhom	6K, S26
10	TFPPy-PDA-COF	✓ ¹⁶	✓	Rhom	6E, S20		17	TPPDA-DMTA-COF	✓ ³¹	✓	Kagome	6L, S27
11	TFPPy-BZ-COF	✓ ²⁷	✓	Rhom	6F, S21		18	PTPA-DMTA-COF	✓	✓	D hexa	6M, S28
12	TFPPy-TPDA-COF	✓ ²⁸	✓	Rhom	6G, S22							
[C ₃ + C ₂]												
19	TAPB-DMTA-COF	✓ ¹¹	✓	Hexa	7A, S29		22	HAPTP-TPA-COF	✓ ³⁴	✓	D trigon	7D, S32
20	TAPB-TPA-COF	✓ ^{24,32}	✓	Hexa	7B, S30		23	HAPTP-BPDC-COF	✓	✓	D trigon	7E, S33
21	TAPT-DMTA-COF	✓ ³³	✓	Hexa	7C, S31		24	HAPTP-TPDC-COF	✓	✓	D trigon	7F, S34
							25	HATN-TPDC-COF	✓	✓	D trigon	7G, S35
[C ₃ + C ₃]												
26	TAPB-TFPB-COF	✓ ^{24,35}	✓	Hexa	7H, S36		28	HAPTP-TAPT-COF	✓	✓	D Rhom	7I, S38
27	TAPT-TPB-COF	✓ ³⁶	✓	Hexa	8B, S37							

Figure 4. Monomers and their combinations. (A) Monomer library. (B) Topology diagrams. (C) Monomer combinations and results for TfOH systems in the synthesis of 28 COFs (Red tick; ticks with sky blue background: new COFs), compared with traditional AcOH systems (blue tick).

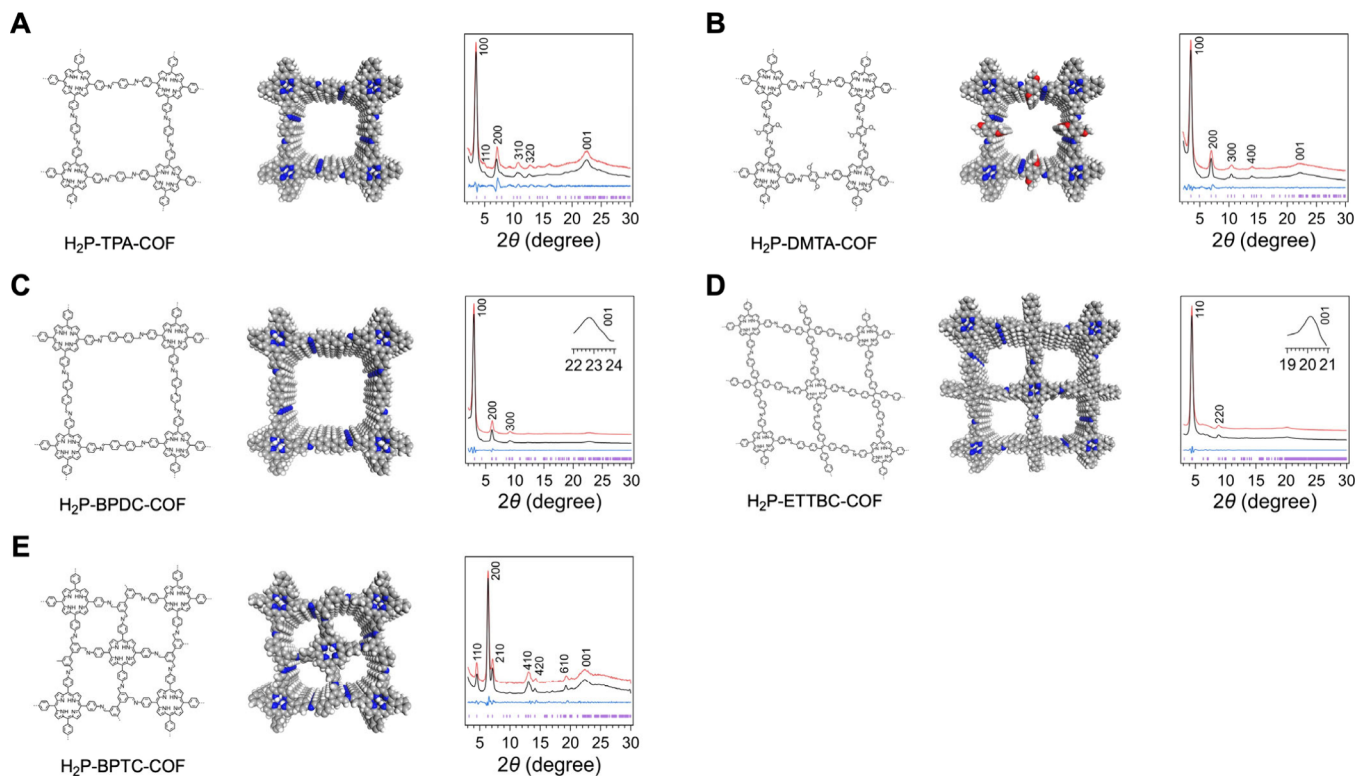


Figure 5. COFs synthesized from the $[C_4 + C_2]$ topology diagram. (A–E) Chemical structure (left), reconstructed structure (middle), and PXRD pattern (black: experimentally observed profiles; red: Pawley refined; blue: differences between Pawley refined and experimental profiles; purple: observed reflections) of (A) H₂P-TPA-COF, (B) H₂P-DMTA-COF, (C) H₂P-BPDC-COF, (D) H₂P-ETTBC-COF, and (E) H₂P-BPTC-COF.

HATN-TPDA-COF, and (110) peak of H₂P-BPTC-COF, respectively) as a measure to evaluate the resultant materials.

(1) Solvent type and scope: We tested almost all solvents that are commonly employed in the COF synthesis (Figure 3A,C,E; Tables S2–S4, Figure S7A). Most alcohols (except isopropanol), including MeOH, EtOH, *n*-propanol, *n*-BuOH, *tert*-BuOH, *n*-pentanol, *n*-hexanol, *n*-octanol, and *n*-decanol, yielded high PXRD intensities and small fwhm, showing distinct differences compared to other nonalcohol solvents such as anisole, acetonitrile (MeCN), benzoyl cyanide (BzCN), dimethylformamide (DMF), dimethylacetamide (DMAc), *N*-methyl-2-pyrrolidone (NMP), mesitylene, *m*-xylene, *p*-xylene, *o*-xylene, toluene, and AcOH (Figure S2A). This is true for all three COFs, as evident by their PXRD patterns (Figure 3A,C,E). Among various alcohols, *n*-BuOH is the best one to achieve the highest PXRD intensity and smallest fwhm for TFPPy-PDA-COF (Figure 3A; Table S2) and HATN-TPDC-COF (Figure 3C; Table S3), while *n*-hexanol is optimal for H₂P-BPTC-COF (Figure 3E; Table S4), as BPTC requires longer chains to enhance their solubility through the acetal protection reaction. *n*-BuOH and *n*-hexanol feature feasible boiling points, high solubility of *in situ* protected monomers, and moderate reactivity with aldehydes. As we set the reaction temperature at 120 °C, MeOH, EtOH, and *n*-propanol are unsuitable, owing to their low boiling points. Meanwhile, *n*-octanol and *n*-decanol are ill-fit due to their low reactivity in acetal formation. Aromatic alcohols such as benzyl alcohol were inapplicable, resulting in amorphous products (Figure 3A). Among nonalcohol solvents, dioxane and *o*-DCB displayed good PXRD intensity and fwhm (Figure S7A), which are however greatly inferior to those of *n*-BuOH.

(2) The amount of solvent: As *n*-BuOH and *n*-hexanol behave best in the synthesis, we tuned their volume to see how it affects the polymerization, by keeping the same amounts of monomers and the same volume ratio of TfOH aqueous solution (0.2 M) with *n*-BuOH (Figure 2B,D,F; Tables S2–S4). Tuning the solvent amount from 0.2 to 1.0 mL or 0.2 to 1.8 mL shows a general tendency that the solvent amount is quite critical. For TFPPy-PDA-COF, a *n*-BuOH of 0.3 mL displays the highest PXRD intensity and the smallest fwhm (Figure 3B). For HATN-TPDC-COF, 1.0 mL of *n*-BuOH leads to the best result (Figure 3D). Notably, H₂P-BPTC-COF attains the highest PXRD peaks and the smallest fwhm in *n*-hexanol (Figure 3F; 0.7 mL).

(3) TfOH concentration: We tuned the TfOH concentration from 0.05 to 1.0 M and the volume ratio from 5 to 40 vol % to reveal the optimal amount for the polymerization of TFPPy-PDA-COF (Table S2; Figure S7B, C). We observed that the concentration of TfOH greatly affects the polymerization. An optimal TfOH concentration is an aqueous solution of 0.2 M with a 10 vol % of alcohol for TFPPy-PDA-COF (Table S2; Figure S7B, C). A low or high concentration decreases both the PXRD intensity and the yield.

(4) Reaction temperature and time: A general tendency is that a high temperature yields a high PXRD intensity and narrow fwhm in a short time. For TFPPy-PDA-COF, reacting at 150 °C reaches the highest PXRD intensity within 1 day, while reacting at 90 or 120 °C reaches the highest PXRD intensity within 3 days, and 15 days are needed for reactions at 60 °C (Table S2; Figure S7D). In addition, TFPPy-PDA-COF cannot be synthesized at room temperature even when the reaction time was extended to 30 days (Table S2; Figure S7D).

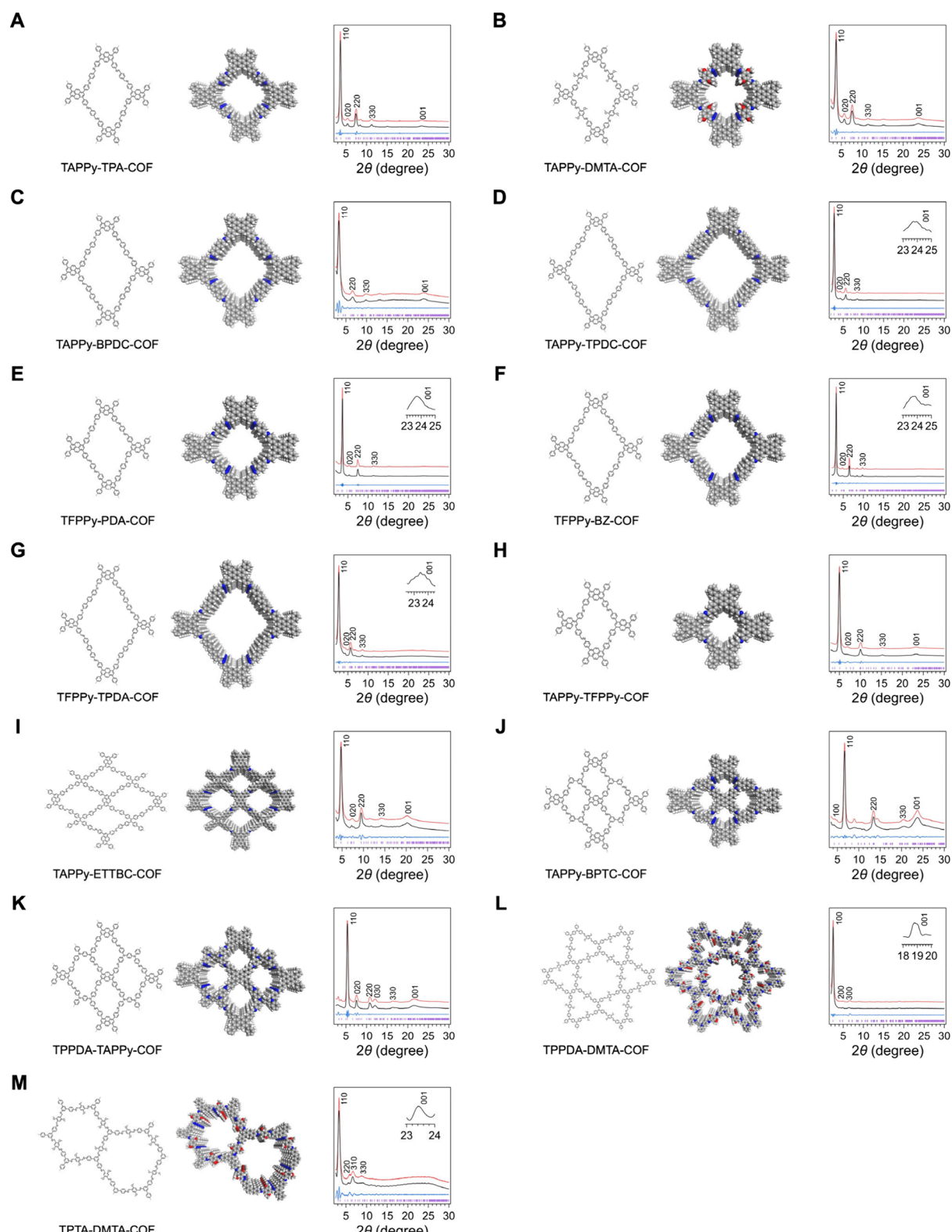


Figure 6. COFs synthesized from the $[C_2 + C_2]$ topology diagram. (A–M) Chemical structure (left), simulated structure (middle), and PXRD patterns (black: experimentally observed profiles; red: Pawley refined; blue: differences between Pawley refined and experimental profiles; purple: observed reflections) of (A) TAPPy-TPA-COF, (B) TAPPy-DMTA-COF, (C) TAPPy-BPDC-COF, (D) TAPPy-TPDC-COF, (E) TFPPy-PDA-COF, (F) TFPPy-BZ-COF, (G) TFPPy-TPDA-COF, (H) TAPPy-TFPPy-COF, (I) TAPPy-ETTBC-COF, (J) TAPPy-BPTC-COF, (K) TPPDA-TAPPy-COF, (L) TPPDA-DMTA-COF, and (M) TPTA-DMTA-COF.

However, for other highly reactive monomer pairs, such as tri(4-aminophenyl)benzene (TAPB) and 2,5-dimethoxyterephthaldehyde (DMTA), highly crystalline TPB-DMTP-COF

was obtained at room temperature for 30 days (Table S5; Figure S10). Through these comparative studies, we set the reaction temperature at 120 °C and reaction time at 3 days.

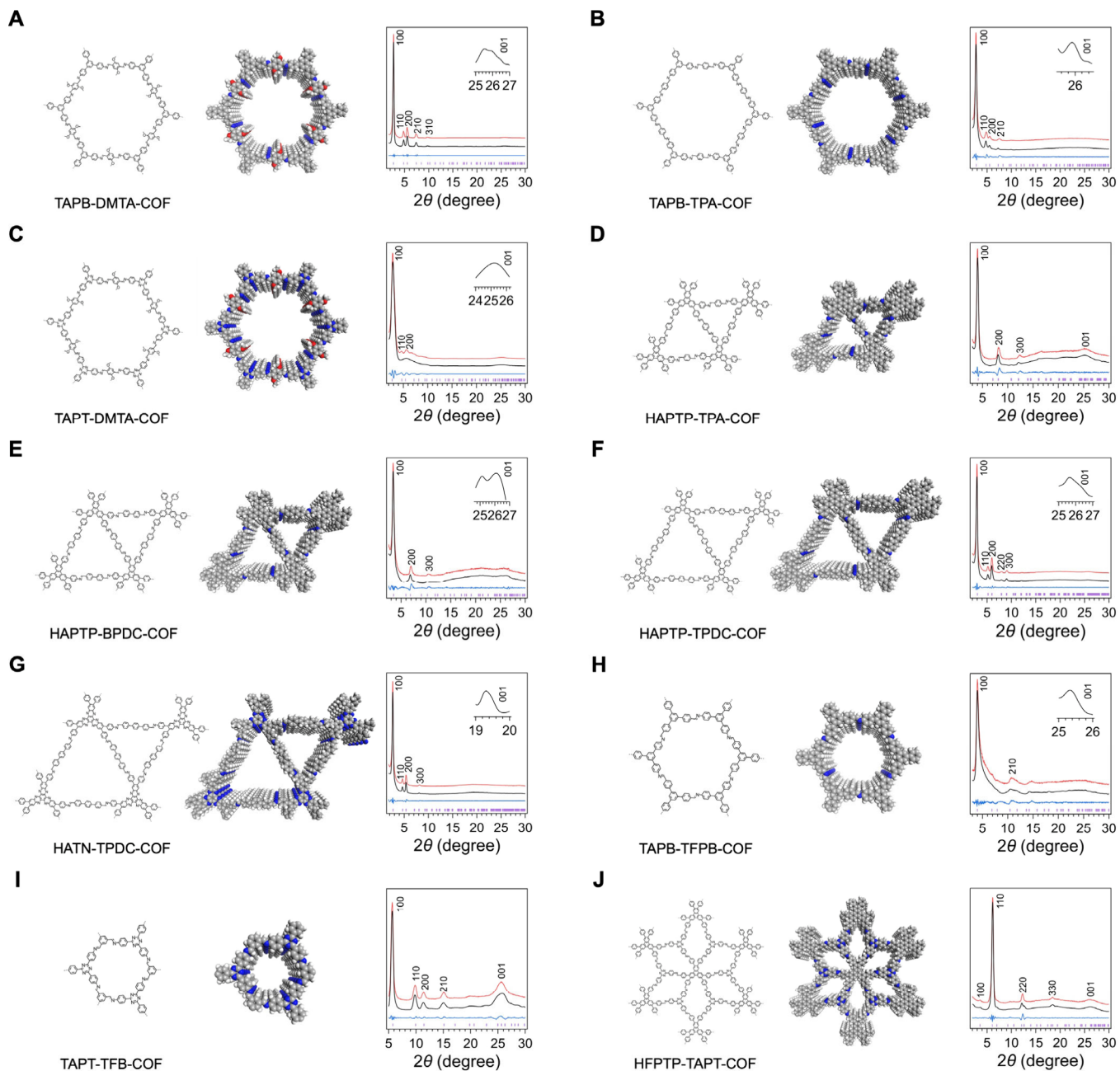


Figure 7. COFs synthesized from the $[C_3 + C_2]$ and $[C_3 + C_3]$ topology diagram. (A–J) Chemical structure (left), simulated structure (middle), and PXRD patterns (black: experimentally observed profiles; red: Pawley refined; blue: differences between Pawley refined and experimental profiles; purple: observed reflections) of (A) TPB-DMTP-COF, (B) TAPB-TPA-COF, (C) TAPT-DMTA-COF, (D) HAPTP-TPA-COF, (E) HAPTP-BPDC-COF, (F) HAPTP-TPDC-COF, (G) HATN-TPDA-COF, (H) TAPB-TFPB-COF, (I) TAPT-TFB-COF, and (J) HFPTP-TAPT-COF.

2.6. Scale-up Experiments. This superacid strategy is capable of a scale-up synthesis. We tested 100-fold scale-up capability under the optimal conditions for the synthesis of TFPPy-PDA-COF (Table S2, Entry S100; Figure S11). This reaction produced 736.2 mg of TFPPy-PDA-COF (91% yield) in one pot, with the same high PXRD intensity of 244.2 k, while the BET surface area is $1606 \text{ cm}^2 \text{ g}^{-1}$ and the pore volume is $0.73 \text{ cm}^3 \text{ g}^{-1}$.

2.7. Scope of In Situ-Protected Strategy. We investigated the scope of the monomer combinations to reveal the generality of this TfOH strategy by fixing the system of *n*-BuOH and TfOH (Figure 4). We developed 11 different amine monomers and 10 aldehyde monomers (Figure 4A) for

the synthesis of 28 imine-linked COFs with different topologies (Figure 4B). We categorized the combinations according to topology diagrams, i.e., $[C_4 + C_2]$, $[C_2 + C_2]$, $[C_3 + C_2]$, and $[C_3 + C_3]$ (Figure 4C), into four different sets to elucidate the polymerization features and the crystallinity and porosity of the resultant COFs. For a specific COF, the reported one through AcOH catalysis is noted with a blue tick ✓ together with reference numbers, while the current TfOH approach is featured by a red tick ✓ along with figure numbers for data. The new COFs that cannot be synthesized by AcOH but were successfully prepared by TfOH are highlighted with sky blue background (✓ red tick with sky blue background).

(1) $[C_4 + C_2]$ topology diagram (Figure 5; Figures S11–S15): We developed 4,4',4'',4'''-(porphyrin-5,10,15,20-tetrayl)tetraaniline (H_2P) as a C_4 -symmetric knot and terephthalaldehyde (TPA), DMTA, [1,1'-biphenyl]-4,4'-dicarbaldehyde (BPDC), 4',4'',4''',4''''-(ethene-1,1,2,2-tetrayl)tetrakis([1,1'-biphenyl]-4-carbaldehyde)) (ETTBC), and [1,1'-biphenyl]-3,3',5,5'-tetracarbaldehyde (BPTC) as C_2 -symmetric units to synthesize five different COFs, i.e., tetragonal H_2P -TPA-COF (Figure 5A; Figure S12), H_2P -DMTA-COF (Figure 5B; Figure S13), and H_2P -BPDC-COF (Figure 5C; Figure S14); dual rhombic H_2P -ETTBC-COF (Figure 5D; Figure S15), and pentagonal H_2P -BPTC-COF (Figure 5E; Figure S16) in *n*-BuOH or *n*-hexanol (0.6–1.0 mL) and TfOH (0.2 M, 60–100 μ L) at 120 °C for 3 days, with yields of 92%, 94%, 91%, 91%, and 95%, respectively. Notably, this TfOH strategy enables the $[C_4 + C_2]$ diagram to synthesize a new pentagonal H_2P -BPTC-COF with an *mcm* topology.

(2) $[C_2 + C_2]$ topology diagram (Figure 6; Figures S17–S28): We have developed C_2 -symmetric amine monomers of 4,4',4'',4'''-(pyrene-1,3,6,8-tetrayl)tetraaniline (TAPPy), benzene-1,4-diamine (PDA), benzi-dine (BZ), [1,1':4',1"-terphenyl]-4,4"-diamine (TPDA), $N^1,N^{1'}$ -(1,4-phenylene)bis(N^1 -(4-aminophenyl)benzene-1,4-diamine) (TPPPDA), and [1,1':3',1"-terphenyl]-4,4",5'-triamine (TPTA) and C_2 -symmetric aldehyde monomers of TPA, DMTA, BPDC, TPDC, 4,4',4'',4'''-(pyrene-1,3,6,8-tetrayl) tetrabenzaldehyde (TFPPPy), ETTBC, and BPTC to enable the polymerization using *n*-BuOH (0.4–1.0 mL)/TfOH (0.2 M, 40–100 μ L) systems at 120 °C for 3 days. As a result, we successfully synthesized 11 COFs with different topologies, including (1) rhombic TAPPy-TPA-COF (Figure 6A; Figure S17, 95% yield), TAPPy-DMTA-COF (Figure 6B; Figure S18, 93% yield), TAPPy-BPDC-COF (Figure 6C; Figure S19, 92% yield), TAPPy-TPDC-COF (Figure 6D; Figure S20, 92% yield), TFPPPy-PDA-COF (Figure 6E; Figure S21, 90% yield), TFPPPy-BZ-COF (Figure 6F; Figure S22, 91% yield), TFPPPy-TPDC-COF (Figure 6G; Figure S23, 92% yield), and TAPPy-TFPPPy-COF (Figure 6H; Figure S24, 95% yield); (2) dual rhombic TAPPy-ETTBC-COF (Figure 6I; Figure S25, 87% yield), TAPPy-BPTC-COF (Figure 6J; Figure S26, 93% yield), and TPPDA-TFPPPy-COF (Figure 6K; Figure S27, 99% yield); (3) kagome TPPDA-DMTA-COF (Figure 6L; Figure S28, 95% yield); and (4) dual hexagonal TPTA-DMTA-COF (Figure 6M; Figure S29, 93% yield). Remarkably, this diagram allows the synthesis of four new COFs, i.e., rhombic TAPPy-TPDC-COF, dual rhombic TAPPy-ETTBC-COF and TAPPy-BPTC-COF, and dual hexagonal TPTA-DMTA-COF, which cannot be synthesized with the AcOH approach.

(3) $[C_3 + C_2]$ topology diagram (Figure 7A–G; Figures S30–S36): We explored C_3 -symmetric amine monomers of TAPB, 4,4',4''-(1,3,5-triazine-2,4,6-triyl)trianiline (TAPT), 4,4',4'',4''',4''''-(triphenylene-2,3,6,7,10,11-hexayl)-hexaaniline (HAPTP), and 4,4',4'',4''',4''''-(diquinoxalino[2,3-a:2',3'-c]phenazine-2,3,8,9,14,15-hexayl)-hexaaniline (HATN) and C_2 -symmetric aldehyde monomers, i.e., DMTA, TPA, BPDC, and TPDC, to investigate the effectiveness of polymerization using *n*-BuOH (0.2–1.2 mL)/TfOH (0.2 M, 20–120 μ L) system at 120 °C for 3 days. We observed that this system produces seven COFs, including (1) hexagonal TPB-DMTP-COF (Figure 7A; Figure S30), TAPB-TPA-COF (Figure 7B; Figure S31), and TAPT-DMTA-COF (Figure 7C; Figure S32) and (2) dual trigonal HAPTP-TPA-

COF (Figure 7D; Figure S33), HAPTP-BPDC-COF (Figure 7E; Figure S34), HAPTP-TPDC-COF (Figure 7F; Figure S35), and HATN-TPDC-COF (Figure 7G; Figure S36) in yields of 94%, 92%, 92%, 98%, 95%, 94%, and 94%, respectively. Notably, this $[C_3 + C_2]$ diagram grows three new dual trigonal COFs, i.e., HAPTP-BPDC-COF, HAPTP-TPDC-COF, and HATN-TPDC-COF.

(4) $[C_3 + C_3]$ topology diagram (Figure 7H–J; Figures S37–S39): We explored C_3 -symmetric amines of TAPB and TAPT and C_3 -symmetric aldehyde of 5'-(4-formylphenyl)-[1,1':3',1"-terphenyl]-4,4"-dicarbaldehyde (TFPB), benzene-1,3,5-tricarbaldehyde (TPB), and 4,4',4'',4''',4''''-(triphenylene-2,3,6,7,10,11-hexayl)hexabenzaldehyde (HFPTP) for synthesizing COFs under the condition of *n*-BuOH (0.2–0.9 mL)/TfOH (0.2 M, 20–90 μ L) at 120 °C for 3 days. We found that these combinations generated (1) hexagonal TAPB-TFPB-COF (Figure 7H; Figure S37) and TAPT-TFB-COF (Figure 7I; Figure S38) and (2) dual rhombic HFPTP-TAPT-COF (Figure 7J; Figure S39) in yields of 95%, 97%, and 95%, respectively. Among them, dual rhombic HFPTP-TAPT-COF is unprecedented.

Through the elaborate synthesis of COFs from different combinations of monomers, we found the following key features:

(1) The optimal system, i.e., *n*-BuOH with 10 vol % TfOH (0.2 M) aqueous solution, 120 °C, and 3 days, performs well as a general condition for imine-linked COFs, while H_2P -BPTC-COF grows well in *n*-hexanol.

(2) For different COFs, the only difference is the solvent amount, while retaining the same 10 vol % catalyst. Generally, hexagonal COFs require a small *n*-BuOH amount of only 0.2 mL, setting a monomer concentration at a range of 0.04–0.06 mmol. Trigonal and tetragonal COFs need more solvent, which is 0.6–1.2 mL for 0.01–0.04 mmol monomers. The solvent volume for rhombic COFs locates at the middle, which is 0.6–1.0 mL for 0.02–0.04 mmol monomers. Table S6 summarizes the conditions for the *in situ* protected synthesis of 28 COFs.

(3) Among these 28 COFs, 9 COFs were synthesized for the first time, including pentagonal H_2P -BPTC-COF, rhombic TAPPy-TPDC-COF; dual rhombic TAPPy-ETTBC-COF, TAPPy-BPTC-COF, and HFPTP-TAPT-COF; dual hexagonal TPTA-DMTA-COF; and dual trigonal HAPTP-BPDC-COF, HAPTP-TPDC-COF, and HATN-TPDC-COF. These results indicate that this TfOH *in situ* protected method not only displays a wide feasibility of imine-linked COFs but also enables the discovery of new COFs.

(4) The *in situ*-protection addresses a common issue of monomers with poor solubility, represented by TFPPPy, ETTBC, BPTC, and HFPTP, because the protection reaction improves the monomer solubility, enabling both polymerization and self-healing.

(5) Benefiting from the protected mechanism and controlled release of functional groups, the TfOH-catalytic condition is unique for mesopore COFs, which usually require special postprocess methods²⁴ or introduce additional interlayer interactions^{11,18,26,27} to avoid the collapse of skeletons and pores when synthesized by the conventional AcOH method. This is true for tetragonal H_2P -BPDC-COF (pore size = 2.5 nm), rhombic TAPPy-BPDC-COF (pore size = 2.2 nm), rhombic TAPPy-TPDC-COF (pore size = 2.6 nm), rhombic TFPPPy-BZ-COF (pore size = 2.5 nm), rhombic TFPPY-

TPDA-COF (pore size = 3.0 nm), and hexagonal TAPB-TPA-COF (pore size = 3.0 nm).

These findings unambiguously demonstrated that the superacid TfOH *in situ*-protected synthesis is versatile and facile for the synthesis of imine-linked COFs.

2.8. Characterization. Fourier transform infrared spectroscopy (FT IR) confirmed a new vibrational band at 1596–1612 cm^{−1}, which was assigned to the imine (C=N) linkages (Figures S12–S39,D). Solid-state ¹³C cross-polarization magic angle spinning nuclear magnetic resonance (CP/MAS NMR) spectroscopies (Figures S40–S49) revealed signals at 159.94, 160.96, 160.78, 160.28, 160.46, 158.76, 156.39, 158.48, and 161.38 ppm, which were assigned to the carbons of the imine linkages of new H₂P-BPTC-COF, TAPPY-TPDC-COF, TAPPY-ETTBC-COF, TAPPY-BPTC-COF, TPTA-DMTA-COF, HAPTP-BPDC-COF, HAPTP-TPDC-COF, HATN-TPDC-COF, and HFPTP-TAPT-COF, respectively.

Thermogravimetric analysis confirmed that these 28 COFs are stable up to 350–440 °C under N₂ atmosphere (Figures S12–S39,E). Scanning electron microscopy (SEM) revealed different morphologies of these COFs (Figures S12–S39,F).

2.9. Crystal Structures. The crystal structures of 28 COFs were revealed by their PXRD patterns (Figures 5–7), by comparison with simulated ones; the lattice parameters after Pawley refinements are summarized in Table S7. We categorized these COFs according to the topology diagrams into four classes.

(1) The [C₄ + C₂] topology diagram develops the next five COFs.

(i) Tetragonal: H₂P-TPA-COF exhibited signals at 3.52°, 4.44°, 7.14°, 10.70°, 12.64°, and 22.60° (Figure 5A), which were assigned to the (100), (110), (200), (310), (320), and (001) facets, respectively. H₂P-DMTA-COF displayed peaks at 3.46°, 6.96°, 10.50°, 14.00°, and 22.10° (Figure 5B), which were attributed to the (100), (200), (300), (400), and (001) facets, respectively. H₂P-BPDC-COF showed signals at 2.98°, 6.14°, 9.18°, and 22.90° (Figure 5C), which were allocated to the (100), (200), (300), and (001) facets, respectively.

(ii) Dual rhombic: H₂P-ETTBC-COF displayed signals at 4.40°, 8.80°, and 20.14° (Figure 5D), which were assigned to the (110), (220), and (001) facets, respectively.

(iii) Pentagonal: H₂P-BPTC-COF exhibited peaks at 4.48°, 6.36°, 7.12°, 13.08°, 14.30°, 19.28°, and 22.40° (Figure 5E), which were allocated to the (110), (200), (210), (410), (420), (610), and (001) facets, respectively. The (210) peak identified that the new H₂P-BPTC-COF adopts a pentagonal *mcm* topology, rather than the tetragonal *sql* or the dual rhombic *cpc* topologies (Figure S40).^{37–40}

(2) The [C₂ + C₂] topology diagram generates the next 11 COFs.

(i) Rhombic: TAPPY-TPA-COF displayed signals at 3.64°, 5.38°, 7.50°, 11.30°, and 23.28° (Figure 6A), which were attributed to the (110), (020), (220), (330), and (001) facets, respectively. TFPPy-DMTA-COF exhibited peaks at 3.76°, 5.74°, 7.66°, 11.34°, and 23.68° (Figure 6B), which were assigned to the (110), (020), (220), (330), and (001) facets, respectively. TAPPY-BPDC-COF displayed signals at 3.28°, 6.64°, 9.90°, and 23.86° (Figure 6C), which were allocated to the (110), (220), (330), and (001) facets, respectively. TAPPY-TPDC-COF exhibited peaks at 2.80°, 3.94°, 5.64°, 8.46°, and 23.96° (Figure 6D), which were assigned to the (110), (020), (220), (330), and (001) facets, respectively. TFPPy-PDA-COF showed signals at 3.76°, 5.32°, 7.44°,

11.24°, and 23.72° (Figure 6E), which were attributed to the (110), (020), (220), (330), and (001) facets, respectively. TFPPy-BZ-COF exhibited peaks at 3.28°, 4.72°, 6.52°, 9.74°, and 23.84° (Figure 6F), which were allocated to the (110), (020), (220), (330), and (001) facets, respectively. TFPPy-TPDA-COF showed signals at 2.78°, 4.28°, 5.70°, 8.58°, and 23.34° (Figure 6G), which were attributed to the (110), (020), (220), (330), and (001) facets, respectively. TAPPY-TFPPy-COF displayed peaks at 5.00°, 6.90°, 10.08°, 15.24°, and 23.22° (Figure 6H), which were assigned to the (110), (020), (220), (330), and (001) facets, respectively.

(ii) Dual rhombic: TAPPY-ETTBC-COF showed peaks at 4.78°, 7.48°, 9.46°, 14.14°, and 20.08° (Figure 6I), which were attributed to the (110), (020), (220), (330), and (001) facets, respectively. TAPPY-BPTC-COF exhibited signals at 4.06°, 6.68°, 14.34°, 20.48°, and 23.72° (Figure 6J), which were assigned to the (100), (110), (220), (330), and (001) facets, respectively. TPPDA-TFPPy-COF displayed peaks at 5.34°, 7.56°, 10.72°, 12.02°, 16.52°, and 21.28° (Figure 6K), which were allocated to the (110), (020), (220), (030), (330), and (001) facets, respectively.

(iii) Kagome: TPPDA-DMTA-COF exhibited signals at 2.52°, 4.90°, 6.44°, and 18.80° (Figure 6L), which were assigned to the (100), (200), (300), and (001) facets, respectively.

(iv) Dual hexagonal: TPTA-DMTA-COF showed peaks at 3.32°, 5.88°, 6.66°, 8.94°, and 23.40° (Figure 6M), which were attributed to the (110), (220), (310), (330), and (001) facets, respectively.

(3) The [C₃ + C₂] topology diagram forms the next seven COFs.

(i) Hexagonal: TPB-DMTP-COF exhibited signals at 2.72°, 4.76°, 5.52°, 7.36°, 9.68°, and 25.62° (Figure 7A), which were assigned to the (100), (110), (200), (210), (310), and (001) facets, respectively. TAPB-TPA-COF displayed peaks at 2.74°, 4.86°, 5.56°, 7.58°, and 25.96° (Figure 7B), which were allocated to the (100), (110), (200), (210), and (001) facets, respectively. TAPT-DMTA-COF showed signals at 2.82°, 4.94°, 5.64°, and 25.22° (Figure 7C), which were attributed to the (100), (110), (200), and (001) facets, respectively.

(ii) Dual trigonal: HAPTP-TPA-COF exhibited peaks at 4.04°, 8.20°, 12.32°, and 25.54° (Figure 7D), which were assigned to the (100), (200), (300), and (001) facets, respectively. HAPTP-BPDC-COF displayed signals at 3.40°, 6.96°, 10.46°, and 26.10° (Figure 7E), which were allocated to the (100), (200), (300), and (001) facets, respectively. HAPTP-TPDC-COF showed peaks at 2.94°, 5.20°, 6.00°, 7.98°, 9.10°, and 25.76° (Figure 7F), which were attributed to the (100), (110), (200), (220), (300), and (001) facets, respectively. HATN-TPDC-COF displayed signals at 2.74°, 4.64°, 5.38°, 8.18°, and 19.80° (Figure 7G), which were assigned to the (100), (110), (200), (300), and (001) facets, respectively.

(4) The [C₃ + C₃] topology diagram yields the following 3 COFs.

(i) Hexagonal: TAPB-TFPB-COF exhibited peaks at 4.00°, 10.52°, and 25.34° (Figure 7H), which were attributed to the (100), (210), and (001) facets, respectively. TAPT-TFB-COF showed signals at 5.66°, 9.82°, 11.42°, 15.08°, and 25.52° (Figure 7I), which were allocated to the (100), (110), (200), (210), and (001) facets, respectively.

(ii) Dual rhombic: HFPTP-TAPT-COF displayed peaks at 3.58°, 6.16°, 12.26°, 18.44°, and 26.06° (Figure 7J), which

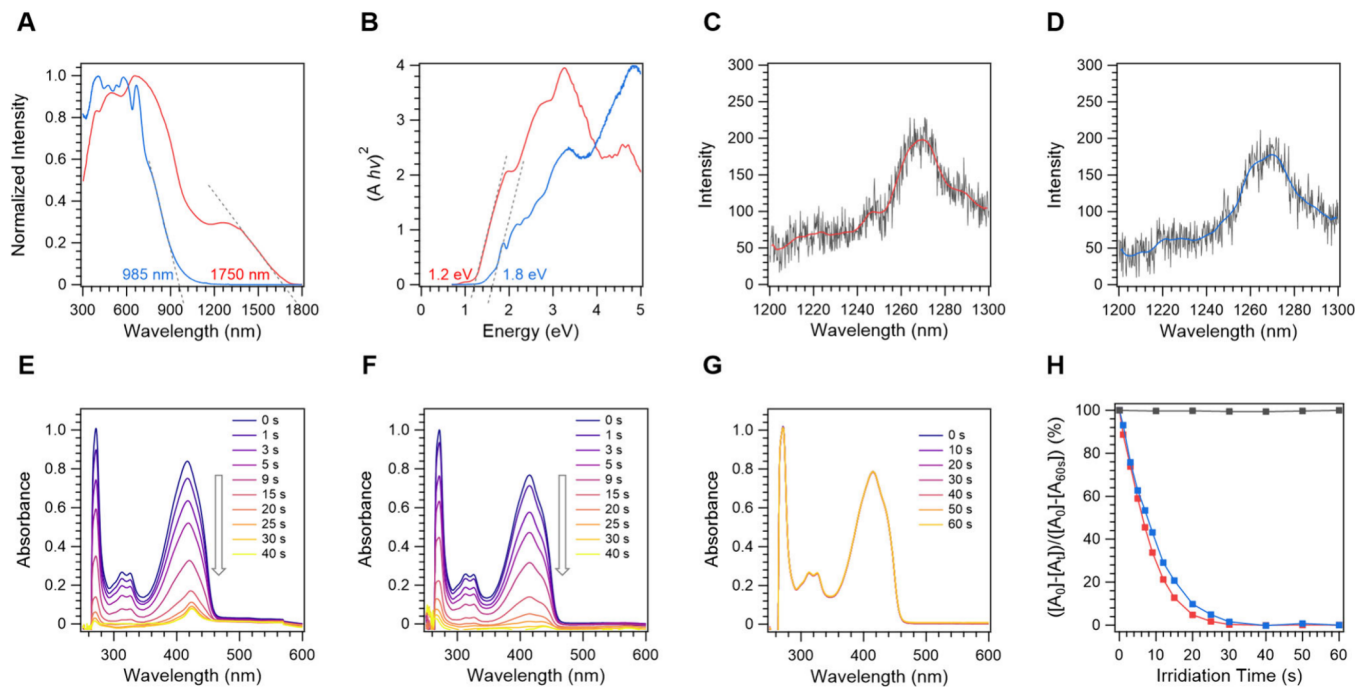


Figure 8. Photocatalytic $^1\text{O}_2$ generation. (A) Solid-state electronic absorption spectrum and (B) Tauc plots of $\text{H}_2\text{P-BPTC-COF}$ (red curves) and $\text{H}_2\text{P-ETTBC-COF}$ (blue curves). (C, D) $^1\text{O}_2$ phosphorescence spectra in $\text{H}_2\text{P-BPTC-COF}$ (C) and $\text{H}_2\text{P-ETTBC-COF}$ (D). (E, F, G) Time profiles of the decomposition of DPBF in the presence of $\text{H}_2\text{P-BPTC-COF}$ (E), $\text{H}_2\text{P-ETTBC-COF}$ (F), and in the absence of COFs (G) under 620 nm irradiation. (H) Conversions of DPBF in the presence of $\text{H}_2\text{P-BPTC-COF}$ (red), $\text{H}_2\text{P-ETTBC-COF}$ (blue), and in the absence of COFs (black).

were attributed to the (100), (110), (220), (330), and (001) facets, respectively.

2.10. Porosity. The porosity was revealed through N_2 sorption isotherm measurements at 77 K. The specific surface area was calculated by the BET method. The nonlocal density functional theory model (NLDFT) was utilized to evaluate the pore size distribution and the pore volume. Their porosity is summarized in Table S8, in comparison with reported imine-linked COFs synthesized from traditional AcOH-catalyzed methods.

(1) $[\text{C}_4 + \text{C}_2]$ topology diagram:

(i) Tetragonal: $\text{H}_2\text{P-TPA-COF}$ displayed a BET surface area of $1483 \text{ m}^2 \text{ g}^{-1}$, a pore volume of $0.49 \text{ cm}^3 \text{ g}^{-1}$, and a pore size of 2.0 nm (Figure S12A–C); $\text{H}_2\text{P-DMTA-COF}$ showed a BET surface area of $938 \text{ m}^2 \text{ g}^{-1}$, a pore volume of $0.33 \text{ cm}^3 \text{ g}^{-1}$, and a pore size of 1.8 nm (Figure S13A–C); $\text{H}_2\text{P-BPDC-COF}$ exhibited a BET surface area of $1052 \text{ m}^2 \text{ g}^{-1}$, a pore volume of $0.49 \text{ cm}^3 \text{ g}^{-1}$, and a pore size of 2.5 nm (Figure S14A–C).

(ii) Dual rhombic: $\text{H}_2\text{P-ETTBC-COF}$ displayed a BET surface area of $1072 \text{ m}^2 \text{ g}^{-1}$, a pore volume of $0.45 \text{ cm}^3 \text{ g}^{-1}$, and pore sizes of 1.1 and 1.9 nm (Figure S15A–C).

(iii) Pentagonal: $\text{H}_2\text{P-BPTC-COF}$ showed a BET surface area of $683 \text{ m}^2 \text{ g}^{-1}$, a pore volume of $0.29 \text{ cm}^3 \text{ g}^{-1}$, and a pore size of 1.0 nm (Figure S16A–C).

(2) $[\text{C}_2 + \text{C}_2]$ topology diagram:

(i) Rhombic: TAPPY-TPA-COF obtained a BET surface area of $1442 \text{ m}^2 \text{ g}^{-1}$, a pore volume of $0.44 \text{ cm}^3 \text{ g}^{-1}$, and a pore size of 2.0 nm (Figure S17A–C); TAPPY-DMTA-COF showed a BET surface area of $636 \text{ m}^2 \text{ g}^{-1}$, a pore volume of $0.20 \text{ cm}^3 \text{ g}^{-1}$, and a pore size of 1.8 nm (Figure S18A–C); TAPPY-BPDC-COF displayed a BET surface area of $756 \text{ m}^2 \text{ g}^{-1}$, a pore volume of $0.22 \text{ cm}^3 \text{ g}^{-1}$, and a pore size of 2.2 nm (Figure S19A–C); TAPPY-TPDC-COF exhibited a BET

surface area of $707 \text{ m}^2 \text{ g}^{-1}$, a pore volume of $0.33 \text{ cm}^3 \text{ g}^{-1}$, and a pore size of 2.6 nm (Figure S20A–C); TFPPY-PDA-COF showed a BET surface area of $2163 \text{ m}^2 \text{ g}^{-1}$, a pore volume of $1.02 \text{ cm}^3 \text{ g}^{-1}$, and a pore size of 2.1 nm (Figure S21A–C); TFPPY-BPDA-COF displayed a BET surface area of $1523 \text{ m}^2 \text{ g}^{-1}$, a pore volume of $0.80 \text{ cm}^3 \text{ g}^{-1}$, and a pore size of 2.5 nm (Figure S22A–C); TFPPY-TPDC-COF obtained a BET surface area of $1300 \text{ m}^2 \text{ g}^{-1}$, a pore volume of $0.71 \text{ cm}^3 \text{ g}^{-1}$, and a pore size of 3.0 nm (Figure S23A–C); TAPPY-TFPPY-COF possessed a BET surface area of $1256 \text{ m}^2 \text{ g}^{-1}$, a pore volume of $0.46 \text{ cm}^3 \text{ g}^{-1}$, and a pore size of 1.6 nm (Figure S24A–C).

(ii) Dual rhombic: TAPPY-ETTBC-COF exhibited a BET surface area of $649 \text{ m}^2 \text{ g}^{-1}$, a pore volume of $0.20 \text{ cm}^3 \text{ g}^{-1}$, and pore sizes of 1.6 and 1.8 nm (Figure S25A–C); TAPPY-BPTC-COF displayed a BET surface area of $783 \text{ m}^2 \text{ g}^{-1}$, a pore volume of $0.28 \text{ cm}^3 \text{ g}^{-1}$, and a pore size of 1.5 nm (Figure S26A–C); TPPDA-TFPPY-COF showed a BET surface area of $1454 \text{ m}^2 \text{ g}^{-1}$, a pore volume of $0.54 \text{ cm}^3 \text{ g}^{-1}$, and a pore size of 1.5 nm (Figure S27A–C).

(iii) Kagome: TPPDA-DMTA-COF obtained a BET surface area of $949 \text{ m}^2 \text{ g}^{-1}$, a pore volume of $0.37 \text{ cm}^3 \text{ g}^{-1}$, and pore sizes of 1.1 and 2.2 nm (Figure S28A–C).

(iv) Dual hexagonal: TPTA-DMTA-COF showed a BET surface area of $777 \text{ m}^2 \text{ g}^{-1}$, a pore volume of $0.25 \text{ cm}^3 \text{ g}^{-1}$, and pore sizes of 1.9 and 2.2 nm (Figure S29A–C).

(3) $[\text{C}_3 + \text{C}_2]$ topology diagram:

(i) Hexagonal: TPB-DMTP-COF exhibited a BET surface area of $1996 \text{ m}^2 \text{ g}^{-1}$, a pore volume of $1.21 \text{ cm}^3 \text{ g}^{-1}$, and a pore size of 3.4 nm (Figure S30A–C); TAPB-TPA-COF showed a BET surface area of $776 \text{ m}^2 \text{ g}^{-1}$, a pore volume of $0.37 \text{ cm}^3 \text{ g}^{-1}$, and a pore size of 3.0 nm (Figure S31A–C); TAPT-DMTA-COF obtained a BET surface area of $1173 \text{ m}^2 \text{ g}^{-1}$, a pore

volume of $0.54 \text{ cm}^3 \text{ g}^{-1}$, and a pore size of 2.8 nm (Figure S32A–C).

(ii) Dual pore trigonal: HAPTP-TPA-COF obtained a BET surface area of $768 \text{ m}^2 \text{ g}^{-1}$, a pore volume of $0.28 \text{ cm}^3 \text{ g}^{-1}$, and pore sizes of 1.1 and 1.9 nm (Figure S33A–C); HAPTP-BPDC-COF showed a BET surface area of $735 \text{ m}^2 \text{ g}^{-1}$, a pore volume of $0.27 \text{ cm}^3 \text{ g}^{-1}$, and pore sizes of 1.2 and 1.6 nm (Figure S34A–C); HAPTP-TPDC-COF exhibited a BET surface area of $1103 \text{ m}^2 \text{ g}^{-1}$, a pore volume of $0.43 \text{ cm}^3 \text{ g}^{-1}$, and pore size of 1.6 and 1.9 nm (Figure S35A–C); HATN-TPDC-COF obtained a BET surface area of $655 \text{ m}^2 \text{ g}^{-1}$, pore volume of $0.22 \text{ cm}^3 \text{ g}^{-1}$, and the pore size of 1.6 and 1.9 nm (Figure S36A–C).

(4) $[C_3 + C_3]$ topology diagram:

(i) Hexagonal: TAPB-TFPB-COF displayed a BET surface area of $628 \text{ m}^2 \text{ g}^{-1}$, a pore volume of $0.25 \text{ cm}^3 \text{ g}^{-1}$, and a pore size of 2.1 nm (Figure S37A–C); TAPT-TFB-COF showed a BET surface area of $1115 \text{ m}^2 \text{ g}^{-1}$, a pore volume of $0.43 \text{ cm}^3 \text{ g}^{-1}$, and a pore size of 1.3 nm (Figure S38A–C).

(ii) Dual rhombic: HFPTP-TAPT-COF obtained a BET surface area of $560 \text{ m}^2 \text{ g}^{-1}$, a pore volume of $0.21 \text{ cm}^3 \text{ g}^{-1}$, and a pore size of 1.1 nm (Figure S39A–C).

These porosity studies disclosed several key findings: (1) These 28 COFs cover a rich library of topologies, i.e., trigonal, tetragonal, rhombic, pentagonal, hexagonal, kagome, dual trigonal, dual rhombic, and dual hexagonal shape, with pore size ranging from micropore to mesopore, i.e., from 1.0 nm ($H_2\text{P-BPTC-COF}$) to 3.4 nm ($TPB\text{-DMTP-COF}$). (2) All 28 COFs exhibited high porosity, compared to the literature (Table S8),^{11,16–36} while featuring a facile synthesis under greatly simplified conditions. Especially, $H_2\text{P-TPA-COF}$, TFPPy-PDA-COF, TFPPy-BZ-COF, and TPPDA-TFPPy-COF reach the highest BET surface areas and pore volumes among reported examples. Remarkably, TPB-DMTP-COF and TFPPy-PDA-COF achieved pore volumes as high as 1.21 and $1.02 \text{ cm}^3 \text{ g}^{-1}$, respectively. (3) Nine new COFs attained high porosity, proving a new way to explore unprecedented porous structures.

2.11. Photocatalytic Singlet Oxygen Generation.

Light-driven activation of molecular oxygen (${}^3\text{O}_2$) into singlet oxygen (${}^1\text{O}_2$), a highly reactive oxygen species, is attracting increasing attention owing to its capability of promoting various reactions. The formation of ${}^1\text{O}_2$ requires energy transfer from the photoexcited triplet state of the COFs to the triplet state ${}^3\text{O}_2$. Making triplet states efficiently in COFs is key to this reaction. We observed that porphyrin COFs, i.e., $H_2\text{P-BPTC-COF}$ and $H_2\text{P-ETTBC-COF}$, are exceptionally active to produce ${}^1\text{O}_2$ under ambient conditions and 620 nm red light irradiation.

We measured the solid-state electronic absorption spectra and calculated optical bandgaps by Tauc plots. Remarkably, $H_2\text{P-ETTBC-COF}$ (Figure 8A, blue curve) exhibited a broad absorption spectrum exceeding 985 nm with an optical bandgap of 1.8 eV (Figure 8B, blue curve). More explicitly, $H_2\text{P-BPTC-COF}$ (Figure 8A, red curve) extends the absorption band even to 1750 nm with a small bandgap of only 1.2 eV (Figure 8B, red curve). These features render $H_2\text{P-ETTBC-COF}$ and $H_2\text{P-BPTC-COF}$ able to harvest infrared light and harness their excited states for ${}^1\text{O}_2$ production.

The singlet ${}^1\text{O}_2$ generation requires a photoexcited triplet state of COFs, which is formed through intersystem crossing from the photoexcited singlet state. We directly proved the generation of ${}^1\text{O}_2$ by phosphorescence spectroscopy. Excitation

of $H_2\text{P-BPTC-COF}$ (Figure 8C) and $H_2\text{P-ETTBC-COF}$ (Figure 8D) in DMF in the presence of oxygen at 620 nm leads to the phosphorescence at $1,270 \text{ nm}$, which is characteristic of ${}^1\text{O}_2$.

We conducted the photocatalytic activity tests using 1,3-diphenylisobenzofuran (DPBF) as the probe for the ${}^1\text{O}_2$ generation, monitored by time-dependent electronic absorption spectroscopy. The system was set as follows: The COF concentration was 0.1 mg mL^{-1} , the DPBF concentration was $4 \times 10^{-5} \text{ M}$, the volume of O_2 -saturated DMF was 3 mL , and the light source was a 620 nm (red) 60 W LED lamp with 0.15 W cm^{-2} light intensity at a 4 cm distance.

Upon 620 nm red light irradiation, $H_2\text{P-BPTC-COF}$ (Figure 8E) and $H_2\text{P-ETTBC-COF}$ (Figure 8F) decomposed DPBF rapidly as evident by the immediate decrease of its absorption band at 415 nm , while control experiments in the absence of COFs presents no spectral change (Figure 8G, Table S9, Figure S50). Remarkably, plotting 415 nm absorbance versus time revealed that $H_2\text{P-BPTC-COF}$ (Figure 8H, red dots) and $H_2\text{P-ETTBC-COF}$ (blue dots) completed the reaction at 30 and 40 s , respectively, showing exceptional photocatalytic activity that is far superior to other reported COFs (Table S10).^{41–49} These results demonstrated that these new COFs are highly photocatalytically active in the production of active oxygen species, driving various transformations and solar-to-chemical energy conversions.

3. CONCLUSION

In summary, we present a novel superacid *in situ*-protected strategy for the synthesis of COFs, by developing TfOH as the catalyst and alcohols as the solvent. This system features (1) protecting amine and aldehyde sites to control the concentration of free amine and aldehyde units for the reaction; (2) improving the solubility of π compounds to reduce aggregations and undesired nucleation as well as the elimination of using aromatic solvents; (3) slowing down the polymerization reaction; and (4) enhancing the reverse self-healing process. Thus, the system becomes simple and controllable, enabling the growth of high-quality COFs.

We detailed the generality of this strategy by applying it to different topology diagrams for monomer combinations, including $[C_4 + C_2]$, $[C_2 + C_2]$, $[C_3 + C_2]$, and $[C_3 + C_3]$, and achieved 28 COFs with high crystallinity and porosity. This study develops trigonal, tetragonal, rhombic, pentagonal, hexagonal, dual trigonal, dual rhombic, and dual hexagonal topologies. Among them, nine new COFs were successfully achieved, which are difficult to prepare with traditional AcOH-catalyzed methods.

We demonstrated that porphyrin COFs serve as low bandgap photocatalysts, which harness red light to efficiently activate molecular oxygen into highly reactive oxygen species ${}^1\text{O}_2$.

With the broad diversity of linkage chemistry, we envision that our strategy is not limited to imine-linked COFs, but it is widely applicable to other COFs. The superacid strategy opens an avenue to unprecedented structures and properties that we have not yet touched.

■ ASSOCIATED CONTENT

● Supporting Information

The Supporting Information is available free of charge at <https://pubs.acs.org/doi/10.1021/jacs.4c17548>.

Methods and characterizations, materials and synthetic methods, including experimental setups, characterization of COFs; supporting tables and figures; atomistic coordinates ([PDF](#))

■ AUTHOR INFORMATION

Corresponding Author

Donglin Jiang – Department of Chemistry, Faculty of Science, National University of Singapore, Singapore 117543, Singapore;  [orcid.org/0000-0002-3785-1330](#); Email: chmjd@nus.edu.sg

Authors

Xingyao Ye – Joint School of National University of Singapore and Tianjin University, Fuzhou 350207, China; Department of Chemistry, Faculty of Science, National University of Singapore, Singapore 117543, Singapore

Ruoyang Liu – Department of Chemistry, Faculty of Science, National University of Singapore, Singapore 117543, Singapore;  [orcid.org/0000-0003-4468-0469](#)

Xinyu Mu – Joint School of National University of Singapore and Tianjin University, Fuzhou 350207, China; Department of Chemistry, Faculty of Science, National University of Singapore, Singapore 117543, Singapore

Shanshan Tao – Department of Chemistry, Faculty of Science, National University of Singapore, Singapore 117543, Singapore

Hao Yang – Joint School of National University of Singapore and Tianjin University, Fuzhou 350207, China; Department of Chemistry, Faculty of Science, National University of Singapore, Singapore 117543, Singapore

Xuejiao J. Gao – College of Chemistry and Materials, Jiangxi Normal University, Nanchang 330022, China;  [orcid.org/0000-0001-7007-4417](#)

Shuo-Wang Yang – Institute of High Performance Computing, Agency for Science, Technology and Research, Singapore 138632, Singapore

Complete contact information is available at:

<https://pubs.acs.org/10.1021/jacs.4c17548>

Author Contributions

[‡]X.Y. and R.L. contributed equally. The manuscript was written through contributions of all authors. All authors have given approval to the final version of the manuscript.

Notes

The authors declare no competing financial interest.

■ ACKNOWLEDGMENTS

D.J. acknowledges Singapore Ministry of Education (MOE) Tier 2 grants (MOE-T2EP10220-0004 and MOE-T2EP10221-0006), MOE Tier 1 grants (A-0008368-00-00 and A-0008369-00-00), and an A* star grant (U2102d2004).

■ REFERENCES

- (1) Geng, K.; He, T.; Liu, R.; Dalapati, S.; Tan, K. T.; Li, Z.; Tao, S.; Gong, Y.; Jiang, Q.; Jiang, D. Covalent Organic Frameworks: Design, Synthesis, and Functions. *Chem. Rev.* **2020**, *120*, 8814–8933.
- (2) El-Kaderi, H. M.; Hunt, J. R.; Mendoza-Cortés, J. L.; Côté, A. P.; Taylor, R. E.; O’Keefe, M.; Yaghi, O. M. Designed Synthesis of 3D Covalent Organic Frameworks. *Science* **2007**, *316*, 268–272.
- (3) Jiang, D. Covalent Organic Frameworks: An Amazing Chemistry Platform for Designing Polymers. *Chem.* **2020**, *6*, 2461–2483.
- (4) Li, Z.; He, T.; Gong, Y.; Jiang, D. Covalent Organic Frameworks: Pore Design and Interface Engineering. *Acc. Chem. Res.* **2020**, *53*, 1672–1685.
- (5) Guan, X.; Chen, F.; Fang, Q.; Qiu, S. Design and Applications of Three Dimensional Covalent Organic Frameworks. *Chem. Soc. Rev.* **2020**, *49*, 1357–1384.
- (6) Li, Y.; Chen, W.; Xing, G.; Jiang, D.; Chen, L. New synthetic strategies toward covalent organic frameworks. *Chem. Soc. Rev.* **2020**, *49*, 2852–2868.
- (7) Deng, L.; Ding, Z.; Ye, X.; Jiang, D. Covalent Organic Frameworks: Chemistry of Pore Interface and Wall Surface Perturbation and Impact on Functions. *Acc. Mater. Res.* **2022**, *3*, 879–893.
- (8) Liu, R.; Tan, K. T.; Gong, Y.; Chen, Y.; Li, Z.; Xie, S.; He, T.; Lu, Z.; Yang, H.; Jiang, D. Covalent Organic Frameworks: An Ideal Platform for Designing Ordered Materials and Advanced Applications. *Chem. Soc. Rev.* **2021**, *50*, 120–242.
- (9) Hu, J.; Huang, Z.; Liu, Y. Beyond Solvothermal: Alternative Synthetic Methods for Covalent Organic Frameworks. *Angew. Chem., Int. Ed.* **2023**, *62* (37), No. e202306999.
- (10) Tan, K. T.; Ghosh, S.; Wang, Z.; Wen, F.; Rodríguez-San-Miguel, D.; Feng, J.; Huang, N.; Wang, W.; Zamora, F.; Feng, X.; et al. Covalent Organic Frameworks. *Nat. Rev. Methods Primers* **2023**, *3*, 1.
- (11) Xu, H.; Gao, J.; Jiang, D. Stable, Crystalline, Porous, Covalent Organic Frameworks as A Platform for Chiral Organocatalysts. *Nat. Chem.* **2015**, *7*, 905–912.
- (12) Li, Z.-J.; Ding, S.-Y.; Xue, H.-D.; Cao, W.; Wang, W. Synthesis of –C≡N– Linked Covalent Organic Frameworks via The Direct Condensation of Acetals and Amines. *Chem. Commun.* **2016**, *52*, 7217–7220.
- (13) Vitaku, E.; Dichtel, W. R. Synthesis of 2D Imine-Linked Covalent Organic Frameworks through Formal Transimination Reactions. *J. Am. Chem. Soc.* **2017**, *139*, 12911–12914.
- (14) Xie, Z.; Wang, B.; Yang, Z.; Yang, X.; Yu, X.; Xing, G.; Zhang, Y.; Chen, L. Stable 2D Heteroporous Covalent Organic Frameworks for Efficient Ionic Conduction. *Angew. Chem., Int. Ed.* **2019**, *58*, 15742–15746.
- (15) Zhao, Y.; Guo, L.; Gándara, F.; Ma, Y.; Liu, Z.; Zhu, C.; Lyu, H.; Trickett, C. A.; Kapustin, E. A.; Terasaki, O.; Yaghi, O. M. A Synthetic Route for Crystals of Woven Structures, Uniform Nanocrystals, and Thin Films of Imine Covalent Organic Frameworks. *J. Am. Chem. Soc.* **2017**, *139*, 13166–13172.
- (16) Tan, K. T.; Tao, S.; Huang, N.; Jiang, D. Water Cluster in Hydrophobic Crystalline Porous Covalent Organic Frameworks. *Nat. Commun.* **2021**, *12*, 6747.
- (17) Wan, S.; Gándara, F.; Asano, A.; Furukawa, H.; Saeki, A.; Dey, S. K.; Liao, L.; Ambrogio, M. W.; Botros, Y. Y.; Duan, X.; Seki, S.; Stoddart, J. F.; Yaghi, O. M. Covalent Organic Frameworks with High Charge Carrier Mobility. *Chem. Mater.* **2011**, *23*, 4094–4097.
- (18) Lin, S.; Diercks, C. S.; Zhang, Y.-B.; Kornienko, N.; Nichols, E. M.; Zhao, Y.; Paris, A. R.; Kim, D.; Yang, P.; Yaghi, O. M.; Chang, J. C. Covalent Organic Frameworks Comprising Cobalt Porphyrins for Catalytic CO₂ Reduction in Water. *Science* **2015**, *349*, 1208–1213.
- (19) Diercks, C. S.; Lin, S.; Kornienko, N.; Kapustin, E. A.; Nichols, E. M.; Zhu, C.; Zhao, Y.; Chang, C. J.; Yaghi, O. M. Reticular Electronic Tuning of Porphyrin Active Sites in Covalent Organic Frameworks for Electrocatalytic Carbon Dioxide Reduction. *J. Am. Chem. Soc.* **2018**, *140*, 1116–1122.
- (20) Hou, Y.; Zhang, X.; Sun, J.; Lin, S.; Qi, D.; Hong, R.; Li, D.; Xiao, X.; Jiang, J. Good Suzuki-Coupling Reaction Performance of Pd Immobilized at The Metal-Free Porphyrin-Based Covalent Organic Framework. *Microporous Mesoporous Mater.* **2015**, *214*, 108–114.
- (21) Patra, B. C.; Bhattacharya, S. New Covalent Organic Square Lattice Based on Porphyrin and Tetraphenyl Ethylene Building Blocks toward High-Performance Supercapacitive Energy Storage. *Chem. Mater.* **2021**, *33*, 8512–8523.
- (22) Yue, J.-Y.; Wang, Y.-T.; Wu, X.; Yang, P.; Ma, Y.; Liu, X.-H.; Tang, B. Two-Dimensional Porphyrin Covalent Organic Frameworks

- with Tunable Catalytic Active Sites for The Oxygen Reduction Reaction. *Chem. Commun.* **2021**, *57*, 12619–12622.
- (23) Auras, F.; Ascherl, L.; Hakimioun, A. H.; Margraf, J. T.; Hanusch, F. C.; Reuter, S.; Bessinger, D.; Döblinger, M.; Hettstedt, C.; Karaghiosoff, K.; et al. Synchronized Offset Stacking: A Concept for Growing Large-Domain And Highly Crystalline 2D Covalent Organic Frameworks. *J. Am. Chem. Soc.* **2016**, *138*, 16703–16710.
- (24) Zhu, D.; Zhang, J.-J.; Wu, X.; Yan, Q.; Liu, F.; Zhu, Y.; Gao, X.; Rahman, M. M.; Yakobson, B. I.; Ajayan, P. M.; Verduzco, R. Understanding Fragility and Engineering Activation Stability in Two-Dimensional Covalent Organic Frameworks. *Chem. Sci.* **2022**, *13*, 9655–9667.
- (25) Guo, M.; Jayakumar, S.; Luo, M.; Kong, X.; Li, C.; Li, H.; Chen, J.; Yang, Q. The Promotion Effect Of π - π Interactions in Pd Nps Catalysed Selective Hydrogenation. *Nat. Commun.* **2022**, *13*, 1770.
- (26) Leng, W.; Peng, Y.; Zhang, J.; Lu, H.; Feng, X.; Ge, R.; Dong, B.; Wang, B.; Hu, X.; Gao, Y. Sophisticated Design of Covalent Organic Frameworks with Controllable Bimetallic Docking for a Cascade Reaction. *Chem.—Eur. J.* **2016**, *22*, 9087–9091.
- (27) Yan, X.; Wang, B.; Ren, J.; Long, X.; Yang, D. An Unsaturated Bond Strategy to Regulate Active Centers of Metal-Free Covalent Organic Frameworks for Efficient Oxygen Reduction. *Angew. Chem., Int. Ed.* **2022**, *61*, No. e202209583.
- (28) Huang, N.; Wang, P.; Addicoat, M. A.; Heine, T.; Jiang, D. Ionic Covalent Organic Frameworks: Design of a Charged Interface Aligned on 1D Channel Walls and Its Unusual Electrostatic Functions. *Angew. Chem., Int. Ed.* **2017**, *56*, 4982–4986.
- (29) Wang, Y.; Cheng, Y.-Z.; Wu, K.-M.; Yang, D.-H.; Liu, X.-F.; Ding, X.; Han, B.-H. Linkages Make a Difference in the Photoluminescence of Covalent Organic Frameworks. *Angew. Chem., Int. Ed.* **2023**, *62*, No. e202310794.
- (30) El-Mahdy, A. F.; Mohamed, M. G.; Mansoure, T. H.; Yu, H.-H.; Chen, T.; Kuo, S.-W. Ultrastable Tetraphenyl-P-Phenylenediamine-Based Covalent Organic Frameworks as Platforms for High-Performance Electrochemical Supercapacitors. *Chem. Commun.* **2019**, *55*, 14890–14893.
- (31) Krishnaraj, C.; Sekhar Jena, H.; Bourda, L.; Laemont, A.; Pachfule, P.; Roeser, J.; Chandran, C. V.; Borgmans, S.; Rogge, S. M. J.; Leus, K.; Stevens, C. V.; Martens, J. A.; Speybroeck, V. V.; Breynaert, E.; Thomas, A.; Voort, P. V. D. Strongly Reducing (Diarylarnino)benzeneBased Covalent Organic Framework for Metal-Free Visible Light Photocatalytic H_2O_2 Generation. *J. Am. Chem. Soc.* **2020**, *142*, 20107–20116.
- (32) Matsumoto, M.; Dasari, R. R.; Ji, W.; Ferriante, C. H.; Parker, T. C.; Marder, S. R.; Dichtel, W. R. Rapid, Low Temperature Formation of Imine-Linked Covalent Organic Frameworks Catalyzed by Metal Triflates. *J. Am. Chem. Soc.* **2017**, *139*, 4999–5002.
- (33) Zhi, Y.; Li, Z.; Feng, X.; Xia, H.; Zhang, Y.; Shi, Z.; Mu, Y.; Liu, X. Covalent Organic Frameworks as Metal-Free Heterogeneous Photocatalysts for Organic Transformations. *J. Mater. Chem. A* **2017**, *5*, 22933–22938.
- (34) Du, C.; Na, W.; Shao, M.; Shang, S.; Liu, Y.; Chen, J. Self-Templated Synthesis of Triphenylene-Based Uniform Hollow Spherical Two-Dimensional Covalent Organic Frameworks for Drug Delivery. *Chem. Mater.* **2023**, *35*, 1395–1403.
- (35) Kaleeswaran, D.; Vishnoi, P.; Murugavel, R. [3 + 3] Imine and β -ketoenamine Tethered Fluorescent Covalent-Organic Frameworks for CO_2 Uptake and Nitroaromatic Sensing. *J. Mater. Chem. C* **2015**, *3*, 7159–7171.
- (36) Dong, J.; Wang, Y.; Liu, G.; Cheng, Y.; Zhao, D. Isoreticular Covalent Organic Frameworks for Hydrocarbon Uptake and Separation: The Important Role of Monomer Planarity. *CrystEngComm* **2017**, *19*, 4899–4904.
- (37) Pham, H. Q.; Pham-Tran, N.-N. Topological Insulating Phase in Single-Layer Pentagonal Covalent Organic Frameworks: A Reticular Design Using Metal Phthalocyanine. *Chem. Mater.* **2021**, *33*, 4488–4499.
- (38) Wen, F.; Xu, K.; Feng, Y.; Huang, N. Two-Dimensional Covalent Organic Frameworks with Pentagonal Pores. *J. Am. Chem. Soc.* **2024**, *146*, 19680–19685.
- (39) Tian, P.-J.; Han, X.-H.; Qi, Q.-Y.; Zhao, X. Identification of Two-Dimensional Covalent Organic Frameworks With Mcm Topology and Their Application in Photocatalytic Hydrogen Evolution. *Chem. Sci.* **2024**, *15*, 9669–9675.
- (40) Liu, Y.; Yuan, L.; Chi, W.; Han, W.-K.; Zhang, J.; Pang, H.; Wang, Z.; Gu, Z.-G. Cairo Pentagon Tessellated Covalent Organic Frameworks with Mcm Topology for Near-Infrared Phototherapy. *Nat. Commun.* **2024**, *15*, 7150.
- (41) Chen, X.; Addicoat, M.; Jin, E.; Zhai, L.; Xu, H.; Huang, N.; Guo, Z.; Liu, L.; Irle, S.; Jiang, D. Locking Covalent Organic Frameworks with Hydrogen Bonds: General And Remarkable Effects on Crystalline Structure, Physical Properties, and Photochemical Activity. *J. Am. Chem. Soc.* **2015**, *137*, 3241–3247.
- (42) Lin, G.; Ding, H.; Chen, R.; Peng, Z.; Wang, B.; Wang, C. 3D Porphyrin-Based Covalent Organic Frameworks. *J. Am. Chem. Soc.* **2017**, *139*, 8705–8709.
- (43) Liu, S.; Liu, Y.; Hu, C.; Zhao, X.; Pang, M. Boosting The Antitumor Efficacy over A Nanoscale Porphyrin-Based Covalent Organic Polymer via Synergistic Photodynamic and Photothermal Therapy. *Chem. Commun.* **2019**, *55*, 6269–6272.
- (44) Zhao, Y.; Dai, W.; Peng, Y.; Niu, Z.; Sun, Q.; Shan, C.; Yang, H.; Verma, G.; Wojtas, L.; Yuan, D.; et al. A Corrole-Based Covalent Organic Framework Featuring Desymmetrized Topology. *Angew. Chem., Int. Ed.* **2020**, *59*, 4354–4359.
- (45) Ding, L. G.; Wang, S.; Yao, B. J.; Li, F.; Li, Y. A.; Zhao, G. Y.; Dong, Y. B. Wound Healing: Synergistic Antibacterial and Anti-Inflammatory Effects of a Drug-Loaded Self-Standing Porphyrin-COF Membrane for Efficient Skin Wound Healing. *Adv. Healthc. Mater.* **2021**, *10*, 2170035.
- (46) Sun, N.; Jin, Y.; Wang, H.; Yu, B.; Wang, R.; Wu, H.; Zhou, W.; Jiang, J. Photoresponsive Covalent Organic Frameworks with Diarylethene Switch for Tunable Singlet Oxygen Generation. *Chem. Mater.* **2022**, *34*, 1956–1964.
- (47) Shi, T.; Wang, H.; Li, L.; Zhao, Z.; Wang, C.; Zhang, X.; Xie, Y. Enhanced Photostability in Protonated Covalent Organic Frameworks for Singlet Oxygen Generation. *Matter* **2022**, *5*, 1004–1015.
- (48) Weng, Z.; Lin, Y.; Guo, S.; Zhang, X.; Guo, Q.; Luo, Y.; Ou, X.; Ma, J.; Zhou, Y.; Jiang, J.; et al. Site Engineering of Covalent Organic Frameworks for Regulating Peroxymonosulfate Activation to Generate Singlet Oxygen with 100% Selectivity. *Angew. Chem., Int. Ed.* **2023**, *135*, No. e202310934.
- (49) Yin, C.; Ye, X.; Tao, S.; Zhao, D.; Zhi, Y.; Jiang, D. Helicene Covalent Organic Frameworks for Robust Light Harvesting and Efficient Energy Transfers. *Angew. Chem., Int. Ed.* **2024**, *63*, No. e202411558.